Terrain deformation measurements from optical satellite imagery: The MPIC-OPT processing services for geohazards monitoring

Floriane Provost, David Michéa, Jean-Philippe Malet, Enguerran Boissier, Elisabeth Pointal, André Stumpf, Fabrizio Pacini, Marie-Pierre Doin, Pascal Lacroix, Catherine Proy, et al.

Remote Sensing of Environment xxx (xxxx) xxx

Contents lists available at ScienceDirect

Remote Sensing of Environment

journal homepage: www.elsevier.com/locate/rse

Terrain deformation measurements from optical satellite imagery: The MPIC-OPT processing services for geohazards monitoring

Floriane Provost [a,b,*], David Michéa [b,c], Jean-Philippe Malet [b,c,d], Enguerran Boissier [e], Elisabeth Pointal [f], André Stumpf [g], Fabrizio Pacini [e], Marie-Pierre Doin [h], Pascal Lacroix [h], Catherine Proy [i], Philippe Bally [a]

[a] European Space Agency, ESA/ESRIN,Largo Galileo Galilei, 1, IT-00044 Frascati, RM, Italy
[b] Ecole et Observatoire des Sciences de la Terre, CNRS UMS 830 - Université de Strasbourg, 5 rue Descartes, F-67084 Strasbourg, France
[c] Application Satellite Survey, A2S - CNRS/Université de Strasbourg, 5 rue Descartes, F-67084 Strasbourg, France
[d] Institut Terre et Environnement de Strasbourg, CNRS UMR 7063 - Université de Strasbourg, 5 rue Descartes, F-67084 Strasbourg, France
[e] Terradue, Via Giovanni Amendola, 46, IT-00185 Rome, Italy
[f] ForM@Ter - Pôle de Données Terre Solide, Institut de Physique du Globe de Paris, Université Paris Diderot, 35 rue Brion, F-75013 Paris, France
[g] GAF AG, Arnulfstraße 199, 80634 München, Germany
[h] Institut des Sciences de la Terre, CNRS UMR 5275 - Université Grenoble-Alpes, 1381 rue de la Piscine, F-38610 Gières, France
[i] CNES: Centre National d'études Spatiales, 75039 Toulouse, France

ARTICLE INFO

Editor: Jing M. Chen

Keywords:
Satellite optical image correlation
Time-series analysis
Landslide ground deformation
Glacier ice velocity
Co-seismic displacement

ABSTRACT

Measuring terrain deformation over several spatial and temporal scales is relevant for many applications in Earth Sciences (i.e. active faults, volcanoes, landslides or glaciers understanding). The growing volume of freely available data represents nowadays a challenge in terms of storage capacity and computing resources which, together with the complexity of the processing (code parameterization, combination of the image sequences, co-registration of the images) may prevent the exploitation of long time series. We propose here a new version of the Multiple-Pairwise Image Correlation toolbox for processing OPTical images (MPIC-OPT). The toolbox proposes an end-to-end solution to compute the horizontal sub-pixel ground deformation time series from large Sentinel-2 datasets. In addition to time series inversion, several corrections and filtering options are integrated to reduce the noise and improve the accuracy and precision of the measurements. In particular, an automatic jitter correction based on wavelet filtering is proposed. Moreover, the MPIC-OPT service is deployed on the Tier 1.5 High-Performance Computing cluster (e.g. Datacentre/EOST-A2S) of the University of Strasbourg and is accessible on-line through the ESA Geohazards Exploitation Platform (GEP) and the ForM@Ter Solid Earth computing infrastructure with a user-friendly environment to query the satellite data catalogues, parameterize the processing and visualize the outputs. We test the performances of MPIC-OPT on several use cases: the measurement of the co-seismic ground deformation of the 2019 Ridgecrest earthquake sequence (USA), of the rapid motion of the Slumgullion landslide (USA) and of the glaciers of the Mont-Blanc massif (France/Italy). We show that the results of MPIC-OPT are in agreement with in-situ data. The jitter correction significantly improves the precision ($RMSE_{jitter}$=0.3m vs. $RMSE_{nojitter}$=0.5m) and the accuracy ($RMSE_{jitter}$=0.3m vs. $RMSE_{nojitter}$=1.3m) of the measurement of the co-seismic displacement of the Rigdecrest seismic deformation. We show that the precision and accuracy of the terrain deformation estimation depend mainly on the correlation threshold and the temporal matching range parameters and we quantify and discuss their impacts. This work opens new perspectives to monitor automatically surface displacements/velocities of natural hazards over large scales and large periods of time.

* Corresponding author at: European Space Agency, ESA/ESRIN,Largo Galileo Galilei, 1, IT-00044 Frascati, RM, Italy.
E-mail address: floriane.provost@esa.int (F. Provost).

https://doi.org/10.1016/j.rse.2022.112949
Received 3 June 2021; Received in revised form 5 January 2022; Accepted 5 February 2022

1. Introduction

Terrain motion is a parameter used in various fields of Earth sciences for understanding the physical mechanisms controlling volcano, fault, landslide or ice glacier activity, but also for Disaster Risk Management (DRM). Several techniques exist to measure the absolute or relative motion of the ground. Some instruments can be installed in-situ (e.g. GNSS, extensometers) or at proximity of the object of interest (e.g. terrestrial laser scanning, total station) but the installation and maintenance of such instrumentation may be challenging in inaccessible and remote areas. Conversely, space-borne sensing of the Earth surface provides a global coverage and allows measurement over extended areas. Numerous satellite constellations, in particular optical satellite imagery of high spatial resolution are now publicly available such as the Copernicus Sentinels (since 2015 - Gascon et al. (2017); Geudtner et al. (2014)) and the NASA long archive of the Landsat missions (since 1970 - (Wulder et al., 2016)). These archives represent an interesting source of information for ground deformation monitoring because of their high frequency of revisit, their spatial resolution and their open-access data policy.

Terrain motion can be measured from space-borne observations using Synthetic Aperture Radar (SAR) and optical imagery. The two main techniques used in Earth Sciences are a) SAR Interferometry (InSAR; (Gens and Van Genderen, 1996; Massonnet and Feigl, 1998)) and b) optical/SAR pixel tracking; (Michel et al., 1999; Leprince et al., 2007; Amitrano et al., 2019; Dille et al., 2021)). SAR interferometry (InSAR) can provide a measurement of the ground deformation at millimetric accuracy in the Line-of-Sight of the satellite by computing the phase difference between two acquisitions (Massonnet and Feigl, 1998). However, InSAR presents some limitations, in particular for the monitoring of rapid terrain motion (e.g. velocity fields >1 m. yr^{-1}) due to a loss of phase coherence.

Pixel offset tracking can measure surface motion by determining the pixel offset between two acquisitions. It can be applied to both SAR and optical images. For SAR and optical images with different look angles, the technique is sensitive to vertical and horizontal displacements while in the case of optical satellite with off-nadir look angles, the technique is sensitive to displacement in the horizontal plane. Depending on the ground sampling distance, the technique is sensitive to large displacement magnitudes from tens of centimeters to meters. Conversely to InSAR processing chains, most of the studies perform separately each steps (e.g. image query, image matching, correction, filtering and time series inversion) needed to extract the ground deformation. Few algorithms propose an integrated way to perform successively some (Stumpf et al., 2017; Nagy et al., 2019; Millan et al., 2019) or all (Van Wyk de Vries and Wickert, 2020; Ali et al., 2020) of these different steps. Moreover, the proposed algorithms are usually tested and developed for one application (i.e. ice velocity, landslide motion, sand dune velocity, etc.) and their performances and reliability are not tested on other applications.

Two main approaches exist to calculate the offsets between two images: a) the image matching approach that computes a similarity function over a sliding window to determine the new position of an object and b) the optical flow approach that consists in retrieving the object motion by solving the brightness consistency equation for the whole image (Brigot et al., 2016). Image matching consists in measuring the similarity between the images based on the pixel intensity and the use of similarity functions (e.g. Cross-Correlation (CC); Normalized Cross-Correlation (NCC)) calculated in the spatial or in the frequency (Fourier) domains (Heid and Kääb, 2012). It was first tested on satellite data in the early 1990's for the monitoring of ice glaciers (Bindschadler and Scambos, 1991; Scambos et al., 1992). Since that early time, numerous algorithms have been developed such as ImCORR (Fahnestock et al., 1992), ImGRAFT (Messerli and Grinsted, 2015), COSI-Corr (Avouac et al., 2006), CIAS (Kääb and Vollmer, 2000), MicMac (Rosu et al., 2015; Rupnik et al., 2017), and QPEC/Medicis (Cournet et al., 2016). The main difference of these algorithms are their pre- and post-processing options. For example, ImCORR proposes a high-pass and low-pass filtering of the image as well as a Principal Component Analysis (PCA) to reduce the satellite image noise (Fahnestock et al., 2016) while MicMac proposes a regularization function to reduce outliers (Rosu et al., 2015). The formulation of the optical flow problem allows for an estimation of the motion field at the pixel level. Optical Flow has been developed since the 1980's (Horn and Schunck, 1981) and applied to satellite observations for various applications like image co-registration (Brigot et al., 2016) or ice flow motion (Vogel et al., 2012; Altena and Kääb, 2017; Lenzano et al., 2018). However, this approach is currently less used by the geoscience community compared to the image matching approach (Stumpf et al., 2016) and few studies compared the performance of the two approaches.

The volume of available satellite images is rapidly growing and, nowadays, several limitations remain for an operational use of image matching techniques. One of the main limitation comes from the numerous errors (i.e. ortho-rectification error, orbital error or other artifact effects) that propagate into the displacement fields which limits the accuracy of the measurement (Scherler et al., 2008; Stumpf et al., 2018). Then, the growing archive of optical images available also poses various challenges in terms of storage and computing resources. The recent development of online processing platforms is hence an opportunity to provide access to High Performance Computer or Cloud facilities combined with a user-friendly environment to setup the processing parameters and visualize the outputs. Several initiatives exist to provide an open-access to global or regional processing such as the ITS_LIVE MEASUREs dataset (Gardner et al., 2019) for glacier monitoring. However, these datasets do not offer the highest spatial resolution and the coverage to understand local processes.

The objective of this work is to present the new functions of the MPIC-OPT workflow, to test its performances on various application and to compare the choice of the image matching strategy. The workflow is fully tailored for Sentinel-2 images and additional corrections and filters have been implemented such as a jitter correction based on wavelet filtering and the implementation of the inversion of the ground deformation time series. The processing chain is optimized for High Performance Computing and accessible through two online platforms. The workflow has been extensively tested to provide robust results on various application. Three MPIC-OPT services have been tailored according to requirements of three Earth science communities to monitoring the deformation of tectonic faults, glaciers or landslides. The performances of these three versions of the MPIC-OPT workflow are tested for three use cases: i) the co-seismic ground deformation of the 2019 Ridgecrest earthquake sequence (USA), ii) the velocity monitoring of ice glaciers in the Mont-Blanc massif, and iii) the ground deformation monitoring of the Slumgullion landslide (USA). Each of the use cases illustrates one of the new functions of the service. The accuracy and precision of the results are assessed and compared to in-situ measurements.

2. Description of the MPIC-OPT workflow

MPIC-OPT is organized in three modules: 1) the correlation module, 2) the correction and filtering module and 3) the spatio-temporal analysis module (Fig. 1). The user can select either an image correlation algorithm (MicMac; (Rupnik et al., 2017)) or an optical flow approach (GeFolKi; (Brigot et al., 2016)). Further module 3 allows extracting persistent motion from the stack of ground deformation grids and the inversion of the time series. The modules are described in the following sections.

A pre-processing module (i.e. *Download and Pre-processing* in Fig. 1) downloads the Sentinel-2 images, extracts the Copernicus DEM (30 m) for the Area Of Interest (AOI) and apply several masks in order to reduce the computation time. The *Fmask* algorithm (Qiu et al., 2019) is used to classify the pixels of the scene into five categories (clear-view, water,

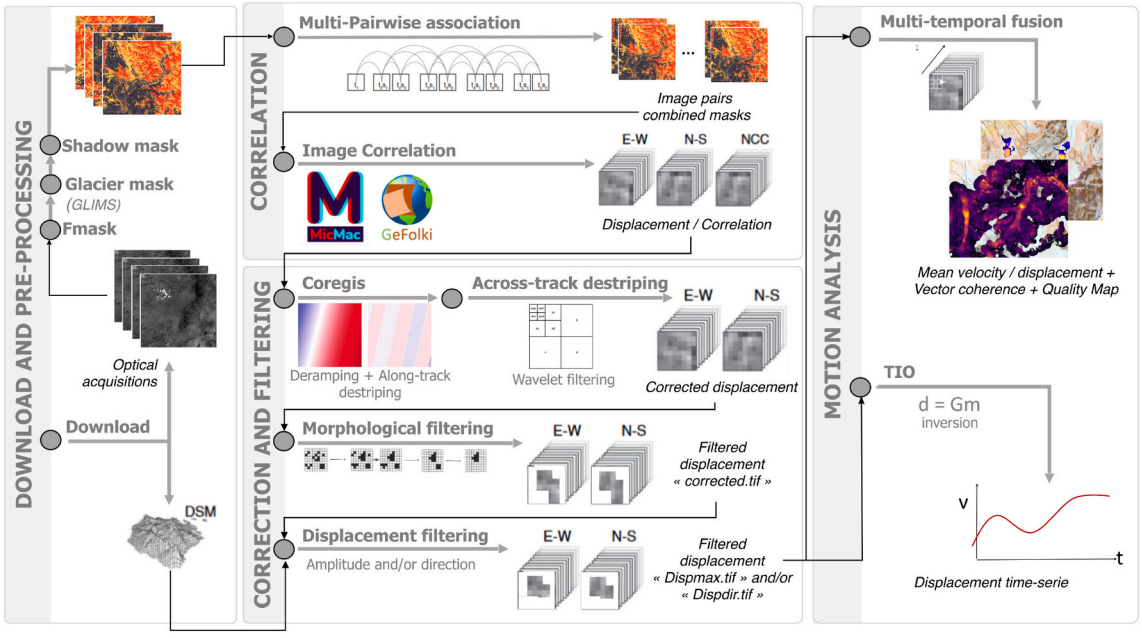

Fig. 1. Diagram representing the different modules of the MPIC-OPT algorithm.

cloud, cloud shadow and snow pixels). Areas covered by clouds, water and snow (optional) can then be removed. The GLIMS database to delineate glacier area (Racoviteanu, 2007) is also available and can be used to reduce the AOI in the case of glacier monitoring. Finally, cast-shadows can be simulated with the DEM and removed to limit the seasonal shifts.

2.1. Module 1: image matching for quantifying ground deformation

Module 1 (i.e. *Correlation* in Fig. 1) is the core module of the MPIC-OPT as it computes the pixel offsets for each image pair. The main function consists in pairing the images and then computing the ground deformation. To create the pairing network, a minimal and maximal matching value must be entered (in days or number of acquisitions) and will define a temporal baseline (in day or number of acquisition). An image pair is then created only if it respects the temporal baseline. There is also an option to create the pairs in both the direction of time ("Forward") and the reverse direction of time ("Backward"). This can be used to improve the accuracy of the results by increasing the Signal-to-Noise Ratio (SNR) (Stumpf et al., 2018). A split-date can be set by the user to enable only the pairing of pre- and post-event images (e.g. excluding the pairing of two pre- or post-event images). This option is designed particularly for co-seismic ground deformation analysis to increase the SNR by only computing the co-seismic pairs.

Once the pairing scheme is set by the user, two algorithms are available to compute the pixel offset for each of the pairs: MicMac (Rupnik et al., 2017) and GeFolki (Brigot et al., 2016). MicMac is an open-source photogrammetric library developed by IGN (Institut National de l'Information Géographique et Forestière, France) that performs image correlation in the spatial domain (Rosu et al., 2015; Le Bivic et al., 2017). The function computes a correlation coefficient on a sliding window and proposes a regularization to stabilize the results especially for small windows sizes (Rosu et al., 2015). The main parameters exposed to the users in the service are the size of the sliding window, the spatial range, the regularization parameter and the correlation threshold. The size of the sliding window controls the amount of details of the computed ground deformation (e.g. a small window allows to retrieve more details of the ground deformation field but may also be more affected by noise). The spatial range corresponds to the expected maximum ground deformation and controls the size of the search area to be matched with the sliding window. The regularization parameter controls the smoothness of the final results (e.g. a high regularization parameter provides smooth ground deformation fields with a low number of outliers). This parameter is highly sensitive and must be chosen carefully. The correlation coefficient gives a measurement of the quality of the similarity of the matched pixels. The correlation threshold allows to remove the pixels with a low correlation (i.e. low similarity). This parameter is used to select pixels for which the measurement is more reliable and also allows to reduce the computation time of the image correlation by removing the pixel with correlation below the threshold. It is also used in the next steps of MPIC-OPT.

The second algorithm available: GeFolki is a non-parametric optical flow toolbox developed by ONERA (French Aeronautics, Space and Defense Research lab). The main parameters exposed to the users are the radius, the number of levels, the number of iterations and the rank. The radius defines the window size on which the matching between the two images will be maximized. In practice, several radii are defined as a power of two in order to increase the robustness of the estimation (Brigot et al., 2016). The number of levels defines the number of layers in the scale-pyramid which corresponds to different levels of down-sampling of the images. The matching function is hence optimized iteratively for each level from the coarser to the finer one taking into account the pixel shift estimation of the precedent level. Because the matching function in the case of optical flow is not linear, several iterations can be needed to approximate the solution. Finally, several filters are applied to the input images to ensure that the images are similar enough to validate the brightness constancy model (Brigot et al., 2016). Among these filters, a rank filter is applied and the rank parameter defines the window size on which the values will be filtered.

The outputs of both algorithms consist in two offset grids in the horizontal plane (North-South, East-West). For MicMac, a third grid is calculated corresponding to a spatial distribution of the correlation coefficient.

2.2. Module 2: correction and filtering of ground deformation

Module 2 is tailored to perform correction of several sources of errors (i.e. orbital error, jitter undulation) and filtering of the displacement fields to remove outliers or inconsistent values.

2.2.1. Deramping and destriping in the along-track direction

Several sources of errors are typically recognizable in the raw ground deformation fields. First, rotational and translational shifts are observed between the input images and result from orbital and ortho-rectification errors of the Sentinel-2 (L1C) data. These shifts could be corrected by accurately reprocessing the raw images (Ding et al., 2016). However neither the Sentinel-2 raw data (L1B) nor the orbital positions of the satellites are available publicly. Post-processing corrections can hence be considered to model and correct these shifts as a linear ramp (Ding et al., 2016; Bontemps et al., 2018; Stumpf et al., 2018):

$$\Delta x_{m,i} = a_x + b_x x_{r,i} + c_x y_{r,i}$$

$$\Delta y_{m,i} = a_y + b_y x_{r,i} + c_y y_{r,i}$$

where $x_{m,\,i}$ and $y_{m,\,i}$ are the modelled offset and $x_{r,\,i}$, $y_{r,\,i}$ are the spatial coordinates of the i^{th} pixel in the ground deformation fields. The coefficient of these planes $a_{x/y}$, $b_{x/y}$, $c_{x/y}$ are estimated by an iteratively reweighted least square (IRLS) with a bi-square loss function minimizing the residuals between the measured and modelled offsets (Stumpf et al., 2018). The modelled offsets are then removed from the raw ground deformation grids.

Secondly, shifts and overlaps are reported for all satellite with embedded pushbroom sensors like Sentinel-2 (Stumpf et al., 2018; Gascon et al., 2017), Landsat-8 (Ding et al., 2016) or Spot-4 (Ayoub et al., 2008). In Sentinel-2 acquisitions, regular stripe artifacts are visible along the track direction in most of the ground deformation fields. This is due to the structure of the image which includes 12 pushbroom sensors that scan the ground along different tracks. In order to correct these effects, Leprince et al. (2008) proposes a pre-processing approach to model and calibrate the charge-coupled device (CCD) shifts as a positionning error of each CCDs sensor. For Spot-4 images, the results show that the CCD shifts can be reduced by one order of magnitude (Leprince et al., 2008). However, this procedure includes a precise coregistration and orthorectification which implies the availability of a reference image with no geometric errors, an accurate DEM and the orbital information (Leprince et al., 2008). The former are not available for Sentinel-2 preventing to accurately model this effect in a pre-processing strategy. (Stumpf et al., 2018) proposes a post-processing methodology to correct the CCD shifts from the ground deformation fields. The mean shift is estimated within each CCD tracks (which footprints are provided in the Sentinel-2 metadata) and subtracted. This strategy is the one implemented in the MPIC-OPT services.

2.2.2. Destripping in the across-track direction to correct jitter vibrations

In some cases, regular across-track undulations are visible in the ground deformation fields. These stripes are usually due to attitude jitter undulation which refers to sensor vibrations due to on-board dynamics of the pushbroom sensors or to external perturbations causing attitude variations. The jitter undulations manifest in the across-track direction at different magnitudes and frequencies depending on the satellites (Ayoub et al., 2008; Teshima and Iwasaki, 2008; Kääb et al., 2016; Nagy et al., 2019; Ye et al., 2019). Jitter variations are present within each acquisition and image correlation creates constructive or destructive combination of these undulations (Kääb et al., 2016). The magnitude of the jitter undulation may be as large as 16 m for Sentinel-2 images (Nagy et al., 2019) and hence, may be an important source of noise for ground deformation analysis. Several approaches can be used to correct this source of noise: COSI-Corr (Avouac et al., 2006) proposes to accurately orthorectify the slave image taking into account the attitude information of the sensor (Scherler et al., 2008). However, if the sampling frequency of the attitude is too low with respect to the acquisition frequency, the modelling of the orbital trajectory will not allow to correct for the jitter undulation (Teshima and Iwasaki, 2008). Moreover, in the case of Sentinel-2, the Level-0 images and orbital information are not available which prevents to consider this approach (Wang and Bürgmann, 2020). Other strategies have been proposed and the most common one consists in computing the average of the ground deformation in the across-track direction (Scherler et al., 2008) and remove it along the across-track direction. However, these corrections need a careful control and a priori knowledge of the stable areas to ensure it does not deteriorate the underlying ground deformation (e.g. co-seismic ground deformation).

The problem of removing stripes within an image is addressed in other scientific domains such as medical imagery for noise filtering (Renier et al., 2016; Kirst et al., 2020). A solution is to use wavelet filtering to remove undulations of a certain frequency and orientation. The python library *pystripe* was initially developed to remove streaks on selective/single plane microscopy images (Kirst et al., 2020). The method consists in applying a discrete wavelet decomposition of the image that returns a coarse approximation of the original image and wavelet coefficients called *detail coefficients*. The *details coefficients* correspond to the high-pass content of the image in the horizontal, vertical and diagonal directions that has been removed from the coarse approximation of the image. The decomposition is repeated recursively on the approximation image. We adapted this library to filter the jitter undulation visible in the ground deformation fields computed with Sentinel-2 images. The choice of the wavelet is critical for the stripe removal. Among the large range of wavelet families available, the Daubechies wavelet family was chosen due to their good trade-off between optimal artifact suppression and high preservation of the original image information reported for similar problems (Münch et al., 2009; Kirst et al., 2020). The first ten Daubechies wavelets have been tested and we observed that the jitter undulations are present only in the horizontal detail coefficient. We also determined that the Daubechie 5 ('db5') is the most suitable wavelet to remove the jitter undulations in Sentinel-2 images without destroying near-fault ground deformation. The corrected deformation field is obtained by reconstructed the diagonal and vertical detail coefficient with the function *waverec2* of the pywavelet library.

2.2.3. Topographic and morphological filtering

Additional topographic and morphological filters are proposed for the monitoring of landslides and glaciers. These filters rely on the assumption that such processes occur along the slope with a rheology that leads to spatially coherent and smooth motion fields in terms of motion direction and amplitude (Stumpf et al., 2017). The main objective is hence to filter out the patches of motion that are incoherent with this assumption. First, a morphological filter is applied by default to remove small isolated motion patches. Opening and closing radius are set to 100 and 200 by default and are not tunable by the user. Secondly, the ground deformation fields are filtered with respect to the slope aspect and the slope angle. The user can filter out a certain range of slope angles. For instance, flat regions (θ<5°) can be filtered out for monitoring landslides in mountainous areas while steep regions (θ>30°) can be filtered out (in certain cases) when studying co-seismic ground deformation to reduce the effects of DEM errors (Kääb et al., 2016). Moreover, the user can decide to filter the motion field according to the aspect of the slope assuming the motion occurs downward in the same orientation as the slope. The maximum angle must be chosen carefully to filter erroneous ground deformation vectors without filtering motion of interest. Two global DEM are currently available to apply the filtering: the MERIT-DEM at 90 m resolution (Yamazaki et al., 2017) and the Copernicus DSM at 30 m resolution.

2.3. Module 3: post-processing of ground deformation for geophysical information retrieval

Module 3 consists in a set of post-processing analysis tools aiming to extract geophysical information from the stack of ground deformation fields. Multi-temporal fusion and time series inversion are performed when activated and are described below.

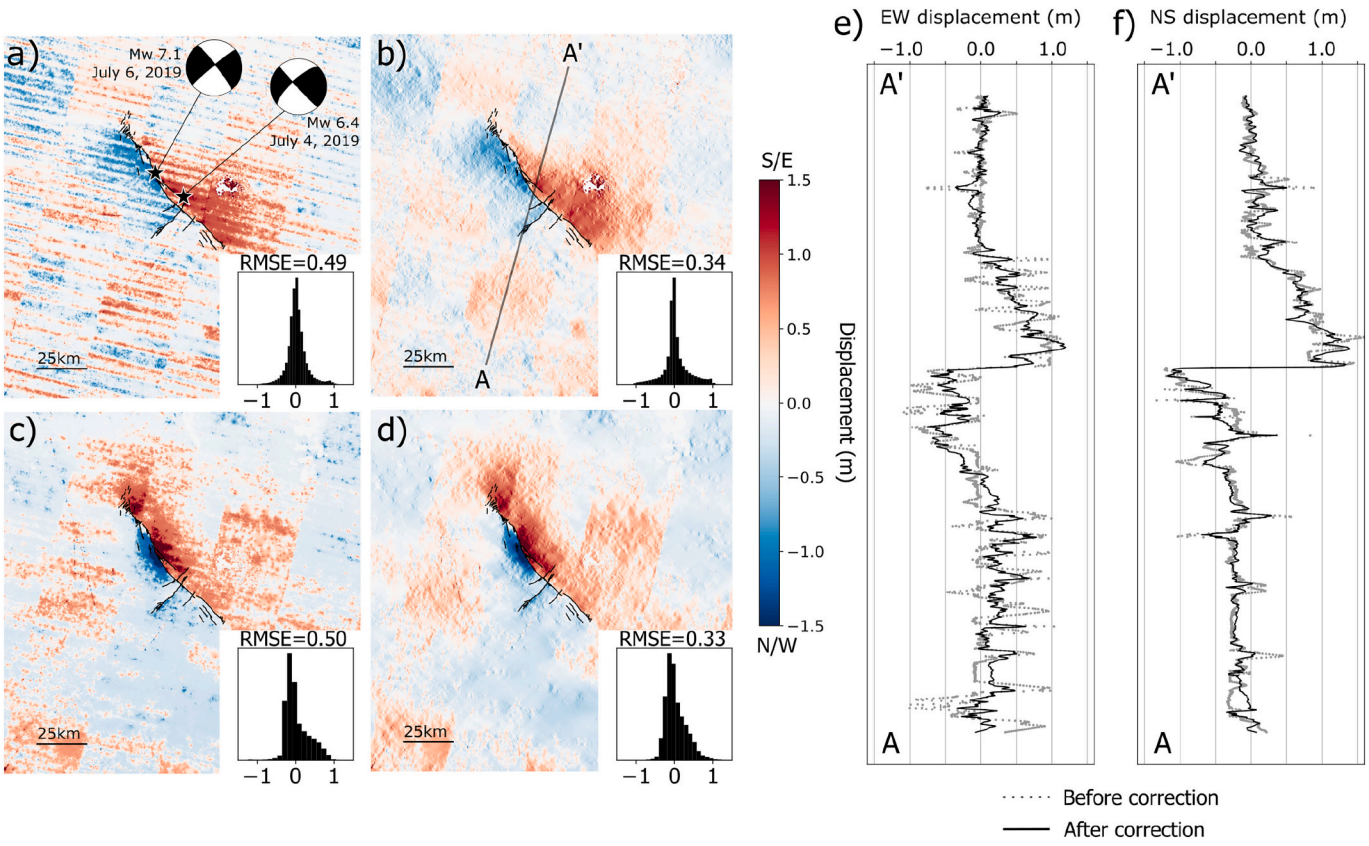

Fig. 2. Effect of wavelet filtering on the NS and EW components of the Ridgecrest earthquake co-seismic ground deformation for a pair of Sentinel-2 images covering the period June 28–July 10, 2020. The EW and NS components before the correction are plotted on subplots a) and c) respectively and after the correction on subplots b) and d). The ground deformation field is plotted along profile AA' for e) the EW and f) the NS component respectively.

2.3.1. *Multi-temporal fusion*

Multi-temporal fusion consists in summarizing the information contained in the stack of the computed ground deformation fields. This tool was developed in the previous version of MPIC (Stumpf et al., 2017). The main indicator of movement consists in computing the mean velocity over the stack of ground deformation. The robustness of this indicator to detect areas in motion depends on the kinematic behavior of the object of interest and the time interval considered to build the image pairs. Indeed the arithmetic mean is particularly suitable in the case the motion is constant over time regardless of the considered time interval between the pairs of images. However, for further detection of active zones, setting a detection threshold on the mean velocity may not be sufficient. Indeed, image correlation may be sensitive to various range of velocities (i.e. cm.day^{-1} to m.day^{-1} for the current archive of Sentinel-2) and setting a threshold on the mean velocity may not mask out numerous active zones. In order to detect these active zones, a second feature is computed by the multi-temporal fusion tool: the Vector Coherence (VC). The VC estimates the coherence of the motion direction over time:

$$VC = \frac{\| \left(\sum_{l=0}^{N} d_l^{EW}\right), \left(\sum_{l=0}^{N} d_l^{NS}\right) \|}{\sum_{l=0}^{N} \| d_l^{EW}, d_l^{NS} \|} \quad (1)$$

It ranges from 0 to 1 with a vector coherence of 1 meaning that the motion occurs along the exact same direction over time (Stumpf et al., 2017; Dehecq et al., 2015) independently of the magnitude of the ground motion. Vector Coherence has been demonstrated to be a relevant indicator to detect unstable areas (Stumpf et al., 2017).

2.3.2. *Time-series inversion module*

Stacks of ground deformation fields (NS, EW) can be inverted to retrieve the ground deformation time series for each pixel of interest. In MPIC-OPT, the inversion is based on the Time-Series Inversion for Optical images algorithm (Bontemps et al., 2018) initially developed to compute time-series of ground deformation from InSAR data (Doin et al., 2011). Considering N optical images, it is possible to create $M < N$ $(N-1)$ pairs. The inversion consists in solving the system of equation for the pixel i:

$$d_i = WG\lambda_i \quad (2)$$

where d_i corresponds to the ground deformation fields computed in module 1 and λ_i corresponds to the incremental ground deformation to be inverted. G is a MxN matrix containing 0 and 1 depending on the network of pairs set up by the user and W is a MxM matrix containing the weights associated to each pair. Weights are chosen to improve the Signal-to-Noise Ratio (SNR) by attributing larger contribution for certain ground deformation fields compared to other considered as less robust. (Lacroix et al., 2019) proposed to weight the pairs with respect to their temporal baseline (ΔT) giving a larger weight to pairs with short baseline assuming less decorrelation. However, it might be considered that pairs with short time separation may not retrieve correctly the slow-motions, given that image matching algorithm have their inherent noise (about $1/10^{th}$ of a pixel-size). We hence propose two different weighting functions:

$$w_l^{short} = \frac{1}{1 + (\Delta T_l - \Delta T_{min})} \quad (3)$$

$$w_l^{long} = \frac{1}{1 + (\Delta T_{max} - \Delta T_l)} \quad (4)$$

where w_l^{short} is a weighting function that gives larger weights to pairs

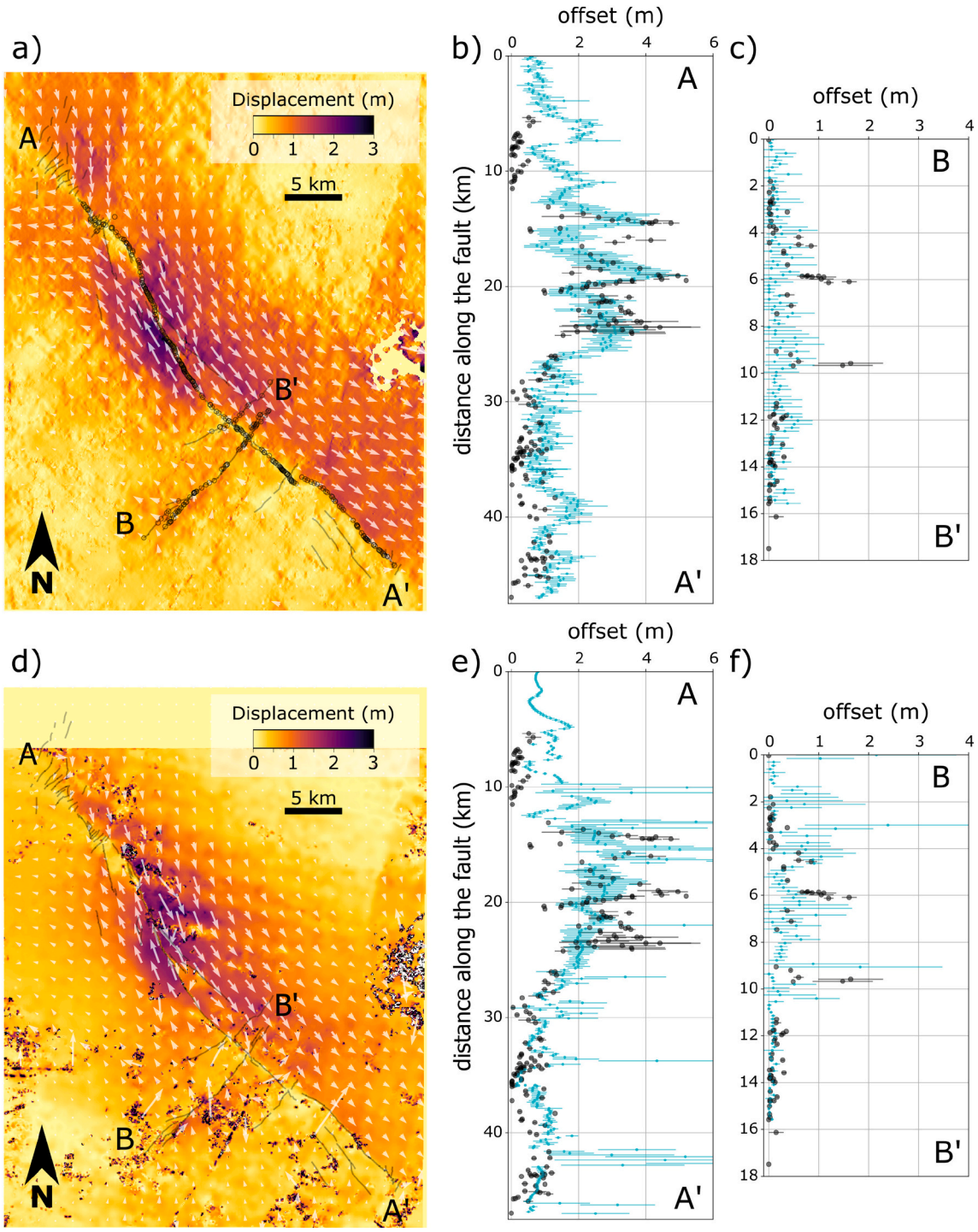

Fig. 3. Comparison of the computed ground deformation fields using MPIC-OPT-ETQ and Cosi-Corr for the Sentinel-2 acquisitions of June 28 and July 10, 2019. The magnitude of the computed horizontal ground deformation (ie. $\sqrt{d_{EW}^2 + d_{NS}^2}$) is plotted for a) MPIC-OPT-ETQ and d) Cosi-Corr (Chen et al., 2020). The horizontal offset at the two main faults AA' and BB' are compared to the field measurements of DuRoss et al., 2020. b) and c) show (in blue) the measured offset and its standard deviation (error bar) using the results of MPIC-OPT-ETQ. e) and f) show (in blue) the measured offset and its standard deviation (error bar) using the results of Cosi-Corr published by (Chen et al., 2020). The field observations (DuRoss et al., 2020) and their uncertainties are plotted in black dots on figures b), c), e) and f) and a). (For interpretation of the references to colour in this figure legend, the reader is referred to the web version of this article.)

with short temporal baselines while w_l^{long} gives larger weights to long temporal baselines. ΔT_l, ΔT_{min} and ΔT_{max} are, respectively, the temporal baselines of the pair l, the minimal and the maximal matching range. Additionally, the grids of correlation coefficient can be used as an additional weight for each pixel and each pair. The system of Eq. (2) is solved by a least-square inversion and in case of rank deficiency with a Singular Value Decomposition (López-Quiroz et al., 2009). Rank deficiency occur when the group of images cannot be linked to another which prevents for the inversion of the system. By default, two iterations are realized including the re-weighting scheme with the network misclosure (Bontemps et al., 2018). The network misclosure $R_i = d_i - G\lambda_i$ is the difference between the ground deformation fields (d_i) and the

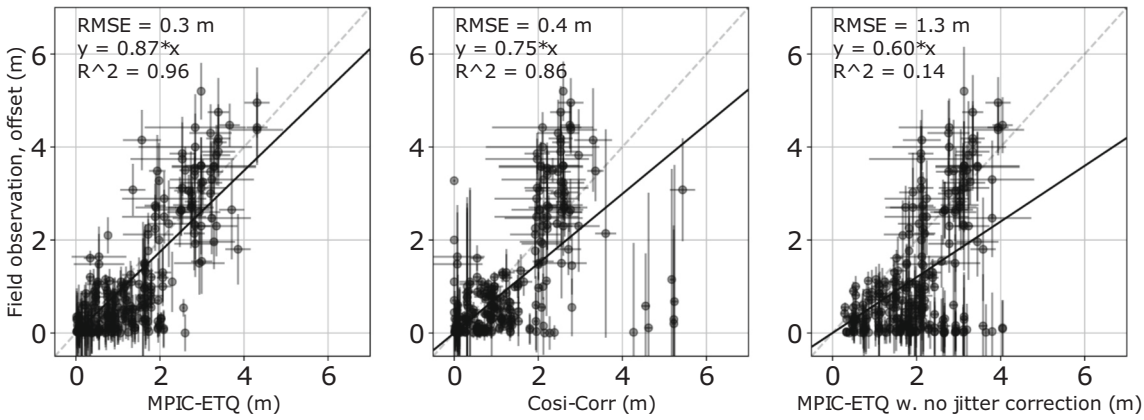

Fig. 4. Comparison between Sentinel-2 derived ground deformation with field observations on profile AA' (DuRoss et al., 2020) for a) MPIC-OPT-ETQ and b) Cosi-Corr (Chen et al., 2020) and c) MPIC-OPT-ETQ when the jitter correction is not performed. The linear function $y = x$ is plotted in grey (dotted line) and the result of the linear regression is plotted in plain black line with the parameters of the regression indicated in the upper left corner. The RMSE between the in-situ measurements and the measure derived by the satellite images is also indicated in the upper left corner.

estimated ground deformation fields after inversion of the incremental ground deformation (λ_i). High values of network misclosure usually indicate inverted ground deformation with large biases and likely wrong estimation of the ground deformation. In order to minimize the influence of these pairs in the second iteration, an additional weight is considered:

$$W_i^j = w_i^* \frac{1}{R_0^2 + R_i^{j2}} \quad (5)$$

where R_0 is a constant that must be approximately equal to the noise standard deviation (Bontemps et al., 2018) and R_i^j is the network misclosure for pixel j and pair i. The inversion procedure is applied independently to the set of North-South and East-West ground deformation pairs. The outputs of the tool provide the incremental ground deformation values at each acquisition date, the mean velocity and the Root Mean Square Error (RMSE) of the ground deformation estimation for each inverted value.

3. Performance of MPIC-OPT for co-seismic, landslide and glacier motion analysis

The MPIC-OPT processing chains is available to the user through three different services: MPIC-OPT-ETQ (EarThQuake), MPIC-OPT-ICE and MPIC-OPT-SLIDE. Each service is tailored for one specific application (i.e. active fault, glacier or landslide monitoring). It means that for each service, a pre-defined succession of the MPIC-OPT functions are run by default. Depending on the service, the user can activate or deactivate some functions or tune the accessible parameters. We present in the next section the results of each service on an application case.

3.1. MPIC-OPT-ETQ: measuring co-seismic motion of the Ridgecrest earthquake sequence, July 2019

In July 2019, several thousands of earthquakes were recorded in Southern California near the town of Ridgecrest close to the Eastern California Shear Zone (ECSZ), the Little Lake Fault zone (LLFZ) and at the East of the San Andreas Fault System (SAF) (Chen et al., 2020; Ross et al., 2019). Two main earthquake events occurred on July 4 and July 6, 2019 (UTC) with magnitudes of Mw 6.4 and Mw 7.1 respectively revealing a complex fault system (Fig. 2). The rupture reached the surface at different locations allowing to map fault system. Various techniques were used to measure the ground motion including direct field measurements (DuRoss et al., 2020), satellite interferometry (Fielding et al., 2020; Xu et al., 2020) and satellite optical image correlation (Milliner and Donnellan, 2020). The focal mechanism (i.e. strike-slip) of the ruptures and the magnitude of the horizontal motion (> 1 m) make offset tracking techniques particularly suitable to measure the co-seismic ground deformation in particular at proximity of the fault line. The technique has been applied to numerous satellite images (i.e. Sentinel-1 (Fielding et al., 2020; Ross et al., 2019), Cosmo-Skymed (Wang and Bürgmann, 2020), Planet (Milliner and Donnellan, 2020) and Sentinel-2 (Chen et al., 2020)). The presence of visible jitter undulations (Chen et al., 2020) and the numerous published results makes this event a good validation site to test MPIC-OPT and the newly implemented jitter correction.

There are two cloudless Sentinel-2 acquisitions before and after the occurrence of the two main ruptures. They are acquired on June 28, 2019 and July 8, 2019 and used to test MPIC-OPT-ETQ. We chosen to work with the MicMac image matching library (Rupnik et al., 2017) on a window size of 5 × 5 pixels with a regularization coefficient of 0.3 and a matching range of 2. Deramping and along-track destriping correction were applied on the ground deformation field as described in Section 2.2.

We first tested the effect of the jitter correction (Fig. 2). The ground deformation fields are strongly affected by sensor jitter undulations (Fig. 2a, c). The effect of the jitter correction on the deformation fields (cf. Section 2.2) are plotted in Fig. 2b, d. The wavelet filtering allows to decrease significantly the RMSE of the North-South and East-West ground deformation fields by 15 cm. The RMSE of the full Sentinel-2 tile is thus ca. 0.35 m against 0.5 m if no jitter correction is applied. The jitter undulations are particularly visible on the EW ground deformation field (Fig. 2a) and are clearly removed after the correction (Fig. 2,b, d and e, f) without loosing the ground deformation signal close to the fault. The CCD stripes remain visible because of undulations along the track direction within each CCD stripes. These undulations remain difficult to remove automatically as their spatial wavelength is of the same magnitude as the one of the co-seismic motion.

The performance of MPIC-OPT-ETQ is further evaluated against other satellite-derived ground deformation products (Chen et al., 2020). We computed the ground deformation for the same pair of images with a regularization parameter of 0.03 to allow for more spatial heterogeneity and capture the ground deformation magnitude at the fault lines. The images were correlated in the forward and backward temporal direction to increase the SNR and the ground deformation fields were averaged. This operation was repeated for the Sentinel-2 bands 2, 3, 4 and 8 (i.e. red, green, blue and infra-red bands). All the ground deformation fields are averaged to obtain the final estimation of the co-seismic ground deformation (Fig. 3a). For comparison, the results of (Chen et al., 2020) obtained with the Cosi-Corr algorithm are plotted on Fig. 3d. The two ground deformation fields are in general agreement for both the

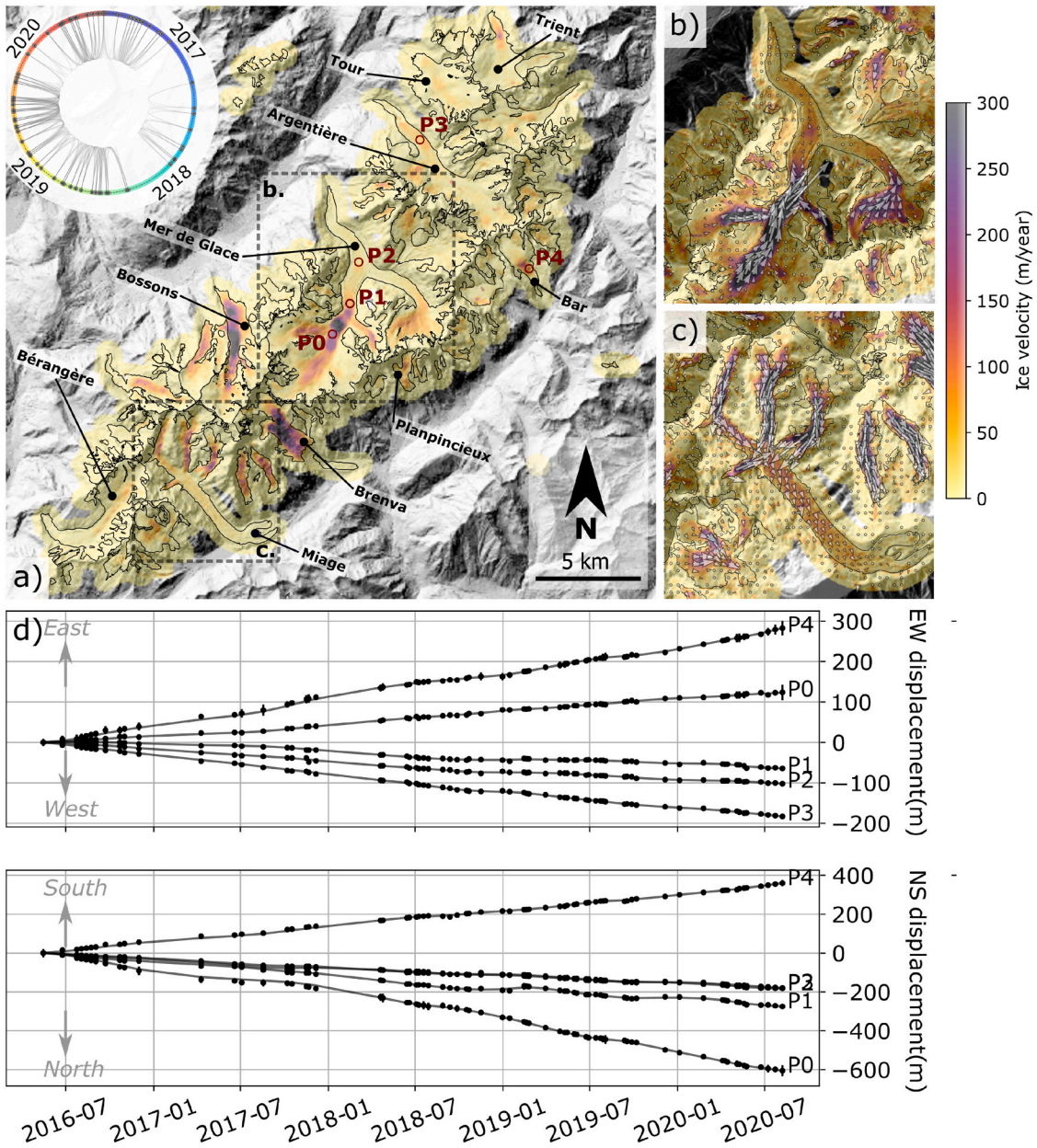

Fig. 5. Results of MPIC-OPT-ICE: a) ice mean velocity ($\sqrt{d_{EW}^2 + d_{NS}^2}$) over the glaciers of the Mont-Blanc massif for the 2015–2020 period; zoom over the Mer de Glace (b) and Miage (c) glaciers with the direction of the ice velocity (white arrows). d) displays the displacement time series for five points located on the Mer de Glace (points P0–2), on the Argentière glacier (point P3) and on the Bar glacier (point P4). The vertical errorbars represent the RMSE of the displacement estimation for each date. The surface velocities are overlaid over the Copernicus 30 m Digital Surface Model (DEM). The upper left Chord circular diagram represents the pairing network between the 70 acquisitions used in the processing (the circle represents the time with the location of each Sentinel-2 acquisition, the black line represents the pairs that were constructed for the processing).

magnitude and direction (Fig. 3a,d). However, the jitter undulations remain visible on the Cosi-Corr results on the Eastern part of the main fault (AA',Fig. 3d) despite the large correlation window (32 × 32 pixels). The RMSE for the MPIC-OPT-ETQ is of 0.48 m versus a RMSE of 0.84 m for the Cosi-Corr results. In general, the MPIC-OPT-ETQ results are less noisy and less contaminated by outliers (Fig. 3a,b) due to the MicMac regularization function (Rosu et al., 2015; Le Bivic et al., 2017) and the jitter correction.

Finally, the MPIC-OPT-ETQ results are compared with field measurements. DuRoss et al. (2020) compiled the measurement taken on the ground along the two faults. They were made by teams of federal, state, academic, and private sector geologists between July and November 2019. These displacement observations describe laterally and/or vertically displaced cultural and geomorphic features (DuRoss et al., 2020). The locations of the field observations used for the comparison are plotted on Fig. 3a. To compare this set of measurements with the results image correlation of Sentinel-2 images, the two main fault lines are simplified (Fig. 3,a,d; profiles A-A' and B-B'). The horizontal offset at the fault is finally computed every 250 m by averaging the ground deformations over 200 m cross-section perpendicular to fault direction. Fig. 3b and c present the ground offset at the fault location computed with MPIC-OPT-ETQ along profile AA' and BB' respectively. Fig. 3e and f present the same results for Cosi-Corr. The field measurements are also plotted for comparison. Both MPIC-OPT-ETQ and Cosi-Corr results show

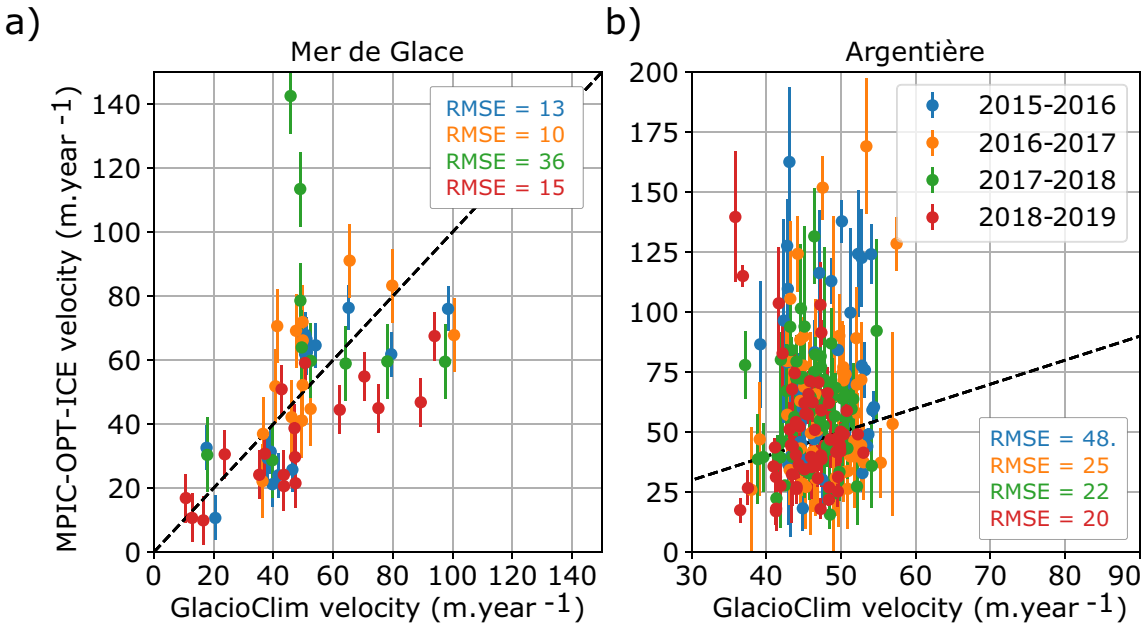

Fig. 6. Comparison between the GlacioClim (glacioclim.osug.fr) and the MPIC-OPT-ICE ice velocity measurements for the Mer de Glace (a) and Argentière (b) glaciers. The black dotted line represent the linear function: y = x. The Root Mean Square Error (RMSE) betweent the GlacioClim and the MPIC-OPT-ICE measurements are indicated in meters per year for each glaciers.

that they can measure accurately the ground offset of the motion occurring on fault AA' (Fig. 3b, e) while the results are less conclusive for fault BB' (Fig. 3c, f). On fault AA', the results of MPIC-OPT-ETQ are significantly better to retrieve the different peaks of deformation occurring in the central part of the fault (between 12 and 28 km, Fig. 3b, e). A linear regression is performed between the field measurements on profile AA' and the results of MPIC-OPT-ETQ (Fig. 4a), Cosi-Corr (Fig. 4b) and MPIC-OPT-ETQ without jitter correction (Fig. 4c). The jitter correction significantly improves the accuracy of the measurement of the ground deformation by reducing the RMSE from 1.3 m (with no jitter correction) to 0.3 m (with the jitter correction). It also shows that MPIC-OPT-ETQ with the jitter correction obtains a reliable estimation of the ground deformation with fewer outliers (regression coefficient of 0.87; R^2=0.96) in comparison with Cosi-Corr (regression coefficients of 0.75; R^2=0.86).

3.2. *Alpine glacier motion in the Mont-Blanc massif from Sentinel-2 image time series*

Several of the most active Mont-Blanc massif glaciers (Brenva, Bossons, Mer de Glace and Argentière) are located in the Mont-Blanc massif (France, Switzerland, Italy). These glaciers are chosen to test the MPIC-OPT chain because their behaviors have been studied (Dehecq et al., 2015; Millan et al., 2019) and instrumented for several decades (GlacioClim: https://glacioclim.osug.fr). A time series of Sentinel-2 images covering the period July 2015 to June 2020 was selected with a cloud-coverage lower than 20%. From this initial selection, a second selection was carried out by inspecting the cloud coverage over the AOI (Supplementary Material, Table 1). The pairs are constructed when the temporal baseline is lower than 100 days and the correlation threshold is set to 0.3. The correlation is performed by MicMac. The temporal baseline is defined to allow comparison with precedent studies (Dehecq et al., 2015; Millan et al., 2019) and to measure the fastest ground motion (i.e. $>100m.\ year^{-1}$). The mean velocity computed by the MPIC-OPT-ICE and the inverted displacement time series are plotted on Fig. 5. The ice velocity ranges from about 50 m.year^{-1} on the lower part of the Argentière glacier to nearly 300 m.year^{-1} in the upper part of the Mer de Glace glacier (Fig. 5a). These velocities are in agreement with previous studies over the same area (Dehecq et al., 2015; Millan et al., 2019). Smaller active glaciers are also visible like the Planpincieux or Bar glaciers (Fig. 5a).

The surface velocities measured with the MPIC-OPT-ICE service are compared to in-situ GNSS campaigns provided by the GlacioClim observatory (glacioclim.osug.fr). The GNSS velocity database consists in differential measurements of targets placed at different locations on the Mer de Glace (10 to 17 targets per year) and Argentière glaciers (40 to 60 targets per year). The measurements are taken two times per year in late summer/early fall. To compare the in-situ observations with the MPIC-OPT-ICE results, we divided the Sentinel-2 dataset into yearly subsets and recomputed the mean velocity. The Sentinel-2 mean velocity is computed as the mean of an area of 3 × 3 pixels around the location of the target positions of the GlacioClim dataset.

Fig. 6 shows the comparison between the MPIC-OPT-ICE and the GlacioClim ice velocity measurements. For the Mer de Glace glacier (Fig. 6a), the two sets of measurements are in fair agreement. The RMSE ranges from 10 to 15 m.year^{-1} and reaches 36 m.year^{-1} in 2017–2018 (Fig. 6a). For the target with the largest velocities (> 90 m.year^{-1}), MPIC-OPT-ICE tends to underestimate magnitude of the displacement by around 20 m.year^{-1}. Several factors can explained this discrepancy: a) for large velocities (> 90 m.year^{-1}), the total displacement measured by the GNSS result from the contribution of different pixels of Sentinel-2, b) the targets with large velocities are located in the upper part of the Mer de Glace where the snow cover prevent for an accurate estimation of the displacement except for during summer months where the glacier velocity is slowing down leading to an underestimation of the velocity. The results on the Argentière glacier are less in agreement with RMSE of 20–25 m.year^{-1} for years, 2016–2017, 2017–2018, 2018–2019 and 48 m.year^{-1} for year 2015–2016. The target of the GlacioClim dataset moves at velocities ranging from 40 to 60 m.year^{-1} while MPIC-OPT-ICE is measuring on the same points velocities ranging from 25 to 175 m. year^{-1}. This bias is observed for every yearly subset and is significantly more important for the year 2015–2016. Similar inaccuracies have been noticed by (Millan et al., 2019) on the Argentière glacier when comparing the velocity from satellite observations and the ones measured by differential GNSS campaign. The Argentière is located at much higher elevations (i.e. 2600 to 3100 m) than the Mer de Glace (<

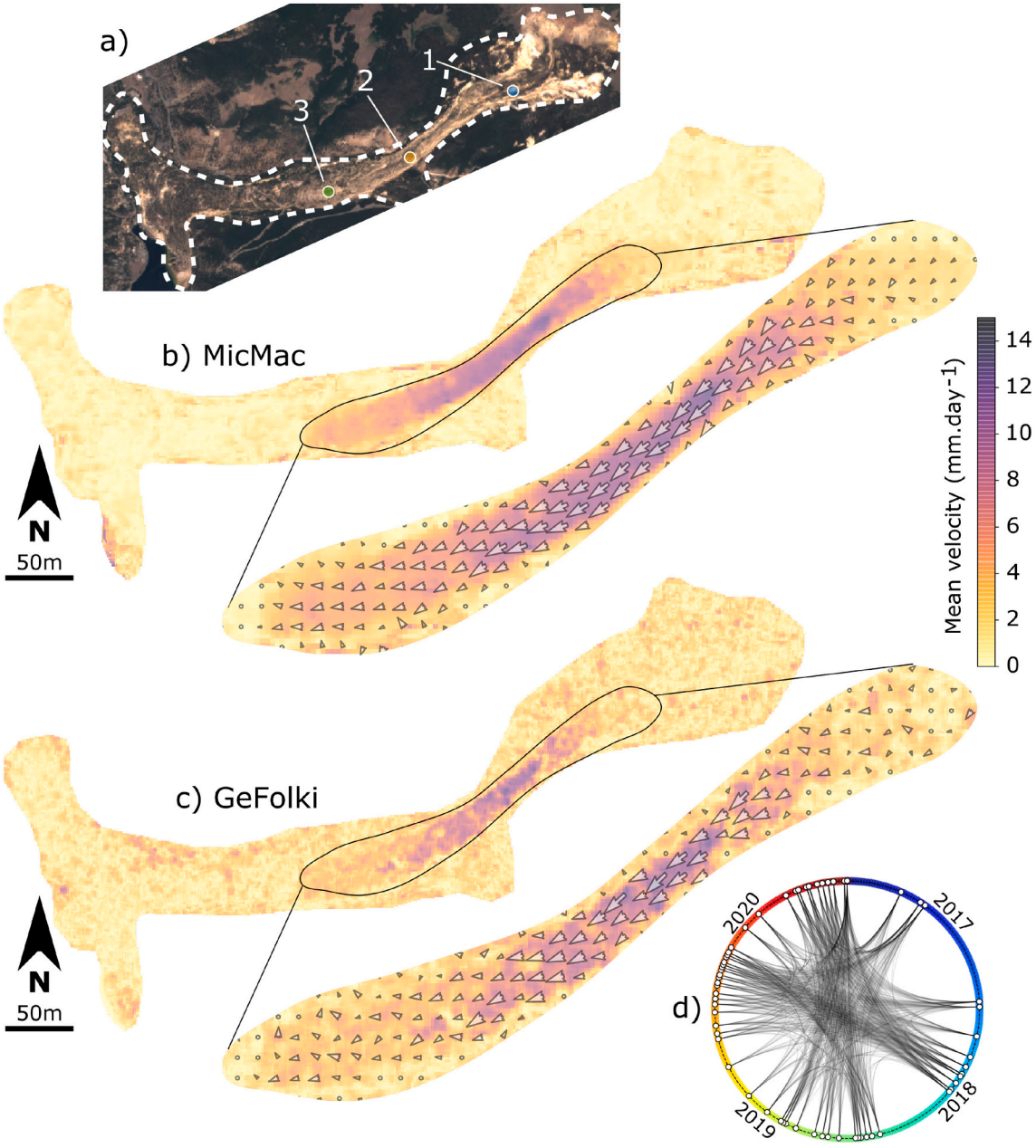

Fig. 7. Results of MPIC-OPT-SLIDE on the Slumgullion landslide for the period 2015–2020. a) shows the landslide limits (white lines) over the Sentinel-2 acquisitions of November 13, 2016. The mean surface velocity computed with MicMac c) and the mean surface velocity computed with GeFolki d). The ground deformation velocity is plotted only within the limits of the landslide. d) is the Chord diagram of the network of Sentinel-2 image pairs (see Fig. 5 caption for more details).

2500 m) resulting in earlier snow cover which prevents the measure of the ice motion for most of the pairs except for the summer months when the glacier is slower. Its surroundings also creates cast shadows masking almost entirely the glacier and prevents the estimation of the displacement for many pairs. Moreover, the surface of the Argentière glacier presents longitudinal features which offers few matching targets to estimate the displacement of the surface. Finally, the temporal baseline of 100 days may be too short to capture the motion of the Argentière glacier.

3.3. *MPIC-OPT-SLIDE: monitoring the ground deformation of the Slumgullion landslide*

The Slumgullion landslide is located in the San Juan Mountains and composed of clay rich materials and volcanic rocks. The landslide is clearly visible on Sentinel-2 images (Fig. 7a) and measures 6.5 km for a width of 0.6 km. Nowadays, a small fraction of the landslide is active at the center (Schulz et al., 2009) and creeps at a velocity of 1–2 cm.day^{-1} (Fleming and US, 1999; Coe et al., 2003; Schulz et al., 2012; Hu et al., 2020). The landslide has been widely studied and its motion is regularly monitored with several instruments (extensometers, GB-InSAR (Schulz et al., 2012), UAVSAR (Hu et al., 2020)). To our knowledge, archives of satellite optical images have not yet been exploited to monitor the slope motion with the exception of (Guerriero et al., 2020). We hence tested the performances of the MPIC-OPT-SLIDE on the Slumgullion landslide (Colorado, USA). The MPIC-OPT-SLIDE service is the version of MPIC-OPT tailored for the monitoring of landslide surface displacement.

The Sentinel-2 archive from 2015 to 2020 offers 97 cloud-free images over the Slumgullion landslide (cf. Supplementary Material, Table 2). The pairs of image were created with a temporal baseline ranging

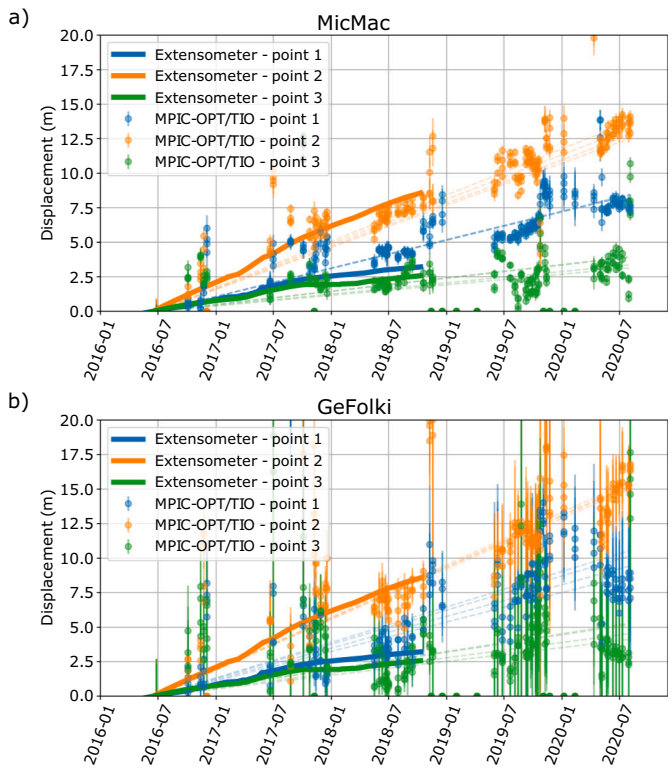

Fig. 8. Comparison between the ground deformation time series of the three extensometers installed on the Slumgullion slope and the MPIC-OPT-SLIDE computation ground deformation time series provided by TIO from the inversion of the MicMac ground deformation grids (a) and GeFolki (b). For each extensometer location, the displacement time series is plotted for the pixel located within 15 m of the extensometers. The dotted lines represents the linear regression computed for each pixel displacement time series. Vertical bars represent the RMS error provided by the inversion.

from 500 days to 1500 days resulting in 853 pairs (Fig. 7d). We computed the ground deformation with MicMac and GeFolki to compare the performance of the two algorithms. The ground deformation time series were inverted and no weight was used in the inversion.

The mean velocity is computed from the stack of the ground deformation grids for MicMac (Fig. 7b) and GeFolki (Fig. 7c). The two results are in agreement with each other and detect the same active area located in the central part of the landslide with a mean velocity of ca. 1.4 cm. day^{-1}. Both the magnitude and the direction of the mean velocity vectors of the two algorithms are in agreement although the extension of the active zone is smaller with GeFolki due to lower velocity magnitude and spatially less coherent vectors (Fig. 7c).

Fig. 8a and b displays the comparison between in-situ measurements with extensometers and the ground deformation time series inverted with TIO from the stack of ground deformation computed with MicMac (Fig. 7a) and GeFolki ((Fig. 7b). The values of the ground deformation time series are plotted for the points surrounding the location of the extensometers (located at less than 20 m) as well as their RMSE provided by the TIO algorithm after inversion. The comparison between the in-situ and the inverted data are possible only between June 2016 (first cloudless acquisition of Sentinel-2) and October 2018 (last acquisition of the USGS extensometers. The results of MicMac (Fig. 8a) and GeFolki (Fig. 8b) are in agreement with each other for the three extensometer locations. However, the GeFolki time series are noisier and RMS errors are larger than the ones obtain with MicMac. The total cumulative ground deformation are slightly larger for GeFolki in comparison with MicMac in particular for point 1 in the central most active part of the landslide with a difference of 2 m. Both methods show good agreement with the in-situ data (Fig. 8a, b) except for point 1 for which the inversion tends to over-estimate the ground deformation for both GeFolki and MicMac dataset.

3.4. Sensor and nominal precision

We use the methodology described in (Millan et al., 2019; Mouginot et al., 2017) to compute the nominal precision and sub-pixel matching precision of the MPIC-OPT algorithm and of the Sentinel-2 images. It consists in computing the distribution of the standard deviation values of the ground deformation grids on stable areas per cycle length (i.e. the temporal baseline between two acquisitions). The median of these distributions is assumed to represent the nominal precision of the sensor for each cycle length (Millan et al., 2019). The sub-pixel image matching precision is computed as $mp = (\sigma_{cycle} * c/ps)$ where σ_{cycle} is the standard deviation of a given cycle, c is the cycle length and ps is the pixel size).

We computed the precision for several cycles and several runs of MPIC-OPT on the Slumgullion landslide and on the Mont-Blanc glaciers. On the Slumgullion landslide we computed the ground deformation grids for cycle length of 0 to 1500 days representing the minimum and maximum cycle length for the Sentinel-2 archive from the end of 2015 to mid-2020. We tested the contribution of the cloud mask, the correlation threshold (c_{min}) and the choice of the matching algorithm (MicMac vs. GeFolki). On the Mont-Blanc glaciers, we computed the ground deformation grids on cycle length ranging from 0 to 400 days and compared the annual ground deformation for each year in order to test the stability of the precision for the Sentinel-2 archive. In both cases, we filtered out the area in motion and estimated the precision on stable zones. For the Mont-Blanc massif, the stable zones are the zones located outside the glacier limits as defined by the GLIMS database. For the Slumgullion landslide, the zones located outside the landslide limits are assumed to be stable (Fig. 8).

We observe for both sites that the nominal precision decreases exponentially with the cycle length (Fig. 9a, b - left). Second order variations are visible on both the nominal and sub-pixel matching precision (Fig. 9). The precision is better for yearly cycle length (i.e. 365, 730, 1095, 1460 days) and increases periodically for inter-season cycles. The precision is the lowest for cycles of 182, 547, 912, 1277 days (Fig. 9a). The amplitude of these variations for the sub-pixel precision is very large for the GeFolki algorithm ($\Delta_{sub-pixel}{}^{mp}$=2.4$px$). For the MicMac correlator, the amplitude of the variations depend on the chosen parameters. The amplitudes are larger in the case of a low correlation threshold (c_min=0.3), with or without cloud mask ($\Delta_{sub-pixel}{}^{mp}$=0.7$px$ and 1.9px respectively). They are less pronounced if the correlation threshold is larger (c_{min}=0.7; $\Delta_{sub-pixel}{}^{mp}$=0.2$px$). Similarly, the mean precision is very large for the GeFolki algorithm ($\mu_{sub-pixel}{}^{mp}$=1.8px) while the MicMac runs have better sub-pixel precision ($\mu_{sub-pixel}{}^{mp}$=0.5px and 0.8px with and without cloud masking respectively for c_{min}=0.3). The best precision is achieved with MicMac when the correlation threshold is large (c_{min}=0.7) with a mean precision of 0.16 pixel. We also observe that the precision of the North-South direction is systematically worse than the East-West direction (Fig. 9) except for the GeFolki algorithm (Fig. 9a, in green). In particular, the mean sub-pixel precision of the Sentinel-2 acquisition is 0.08 pixel for the East-West direction and 0.14 for the North-South direction in the most optimal case (Fig. 9a, in red). The same observations hold for the runs on the Mont-Blanc massif glaciers (Fig. 9b). No significant differences are observed in the ground deformation rates for each year over the Mont-Blanc massif glaciers (Fig. 9b). For this case, the mean sub-pixel precision of the Sentinel-2 acquisition is slightly higher than the one found for the Slumgullion landslide with 0.13 pixel for the East-West direction and 0.19 pixel for the North-South direction (Fig. 9b - right).

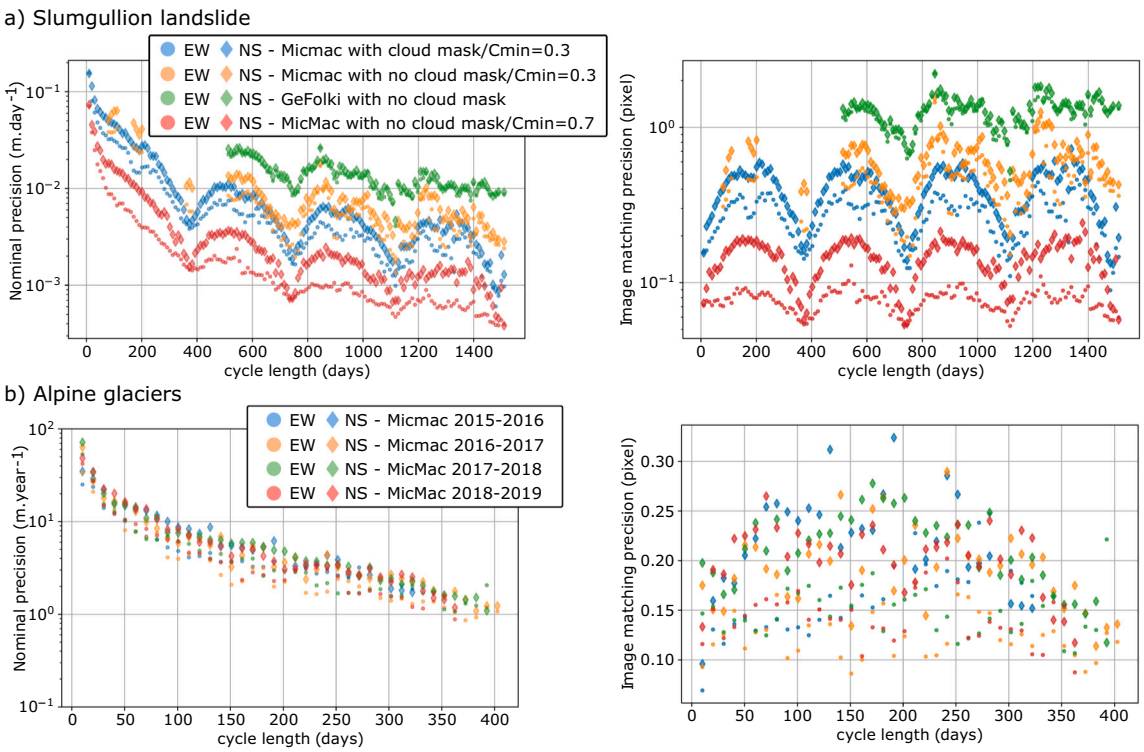

Fig. 9. Nominal precision (left) and sub-pixel matching precision (right) for the Slumgullion landslide (a) and the Alpine glaciers (b). Several options are tested including the comparison between MicMac and GeFolki; the sensitivity to the correlation threshold and cloud masking (a) and the variation of the precision for different years (b).

4. Discussion

4.1. Influence of the jitter correction on the local ground deformation pattern

Nagy et al. (2019) mentioned that jitter undulations were seldom and only observed on two images over 41 images analyzed and that no image with this effect was observed after June 2016 with the new geometrical correction proposed by ESA after that date (Gascon et al., 2017). The example of the Ridgecrest earthquake shows that this effect is still present in Sentinel-2 acquisitions and can drastically affect the exploitation of the Sentinel-2 acquisitions. We thus proposed a correction allowing to remove the jitter undulations observed in the ground deformation fields. The jitter undulations are usually removed by computing their mean amplitude over stable areas (Scherler et al., 2008) and then by removing them over the whole area. This approach poses several problem to be implemented automatically on Sentinel-2 images. First it requires the knowledge of the stable areas which is not necessarily the case; second, in the case of Sentinel-2 acquisitions, the jitter affects individually the different stripes (Fig. 2a, c) making the estimation of the mean amplitude of the jitter undulations and its removal challenging even manually. The proposed correction has the advantage to require no a priori knowledge of the stable area and to perform a filtering over the whole area in a simple manner using the principle of wavelet filtering. Applying the correction improves the precision of the ground deformation fields by decreasing the RMSE (Fig. 2) and removes significantly the number of outliers allowing a better agreement with the field observations (Figs. 3,4). However, the jitter correction is sensitive to the wavelength of the ground deformation pattern and the choice of the wavelet family and rank determines which kind of pattern will be filtered out. In the case of the jitter undulations observed in the Sentinel-2 tile of the Ridgecrest earthquake sequence, we observed a wavelength of 1.8–2.0 km which is in the same order as in Nagy et al. (2019). After the correction, these undulations are removed but we observed large undulations of circa 40 km (or more) resulting in a chessboard-like pattern over the whole tile. Considering a velocity of 7 km.s^{-1} for the satellite, these large undulations correspond to periods of 5.7 s (or more) per undulation. These remaining undulations are difficult to further correct adopting wavelet filtering as they are in the same wavelength as the tectonic ground deformation.

It should be noted that the proposed jitter correction is not advised when the ground deformation pattern of interest is of the same wavelength as the jitter undulations (circa 2 km). This explains why it is not used on the glaciers and landslides services. Also it should be noted that for tectonic ground deformation, the filter can remove small pattern of ground deformation like the one observed in the center of the NW-SE fault (Fig. 10). This pattern of ground deformation is clearly visible on other datasets in particular with Very High Resolution images such as Worldview (Barnhart et al., 2019) or Planet (Milliner and Donnellan, 2020) (Fig. 10). This local ground deformation is likely due to superficial liquefaction and can be observed with Sentinel-2 when the jitter correction is not applied (Fig. 3 d, small subset figure, (Chen et al., 2020)).

4.2. Influence of the correlation parameters and of the pairing network

The accuracy of the terrain motion estimates depends on the service parameterization (Fig. 9). The first obstacle to use image correlation with optical acquisitions is the presence of clouds in the images. Two strategies are tested to remove the clouds in the final results: a) classifying the pixel with *Fmask* to mask out the clouds before the correlation step, b) to set up a high correlation threshold (i.e. c_{min}) to mask out pixels after the correlation. The first option is convenient to reduce the computing time and resources. However, the cloud detection algorithm tends to mask out areas not affected by clouds in particular, snow or fresh landslide outcrops. The second option improves significantly the SNR of the results and the precision (Fig. 9a).

A second critical parameter controlling the success of the processing

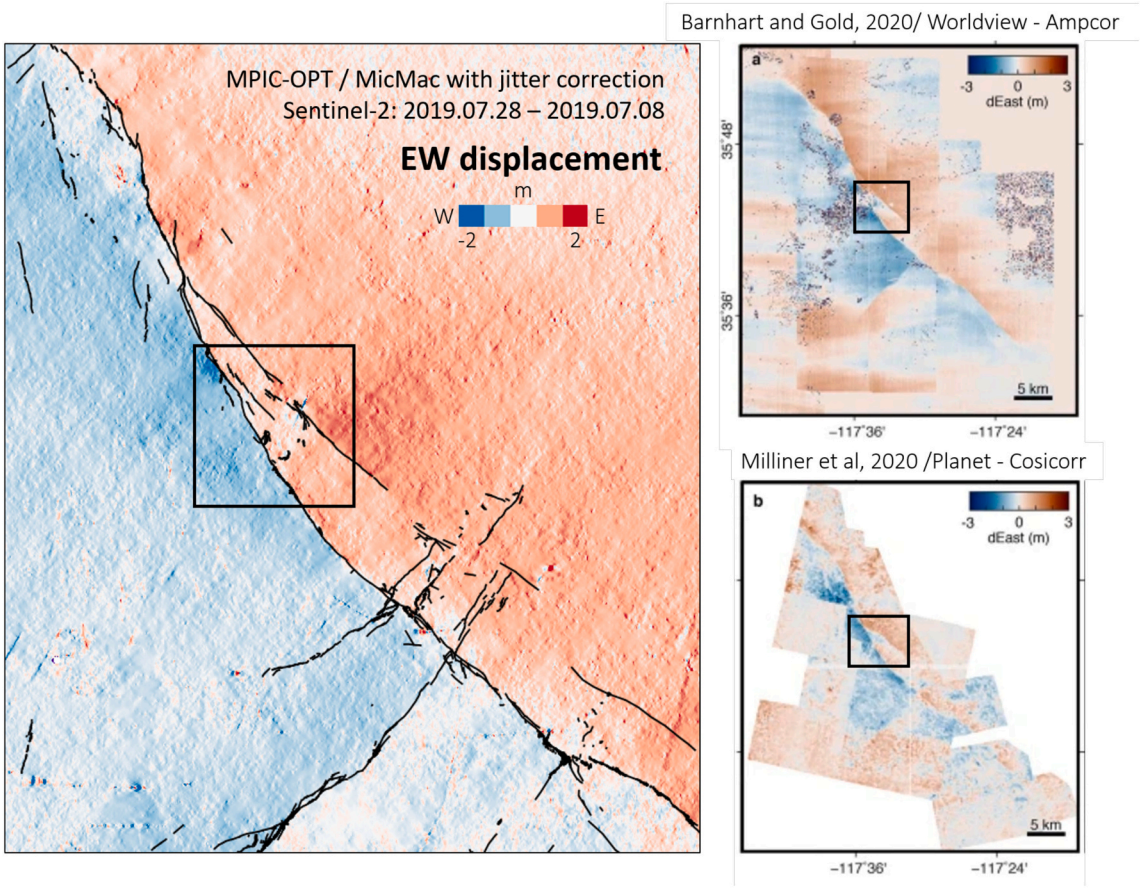

Fig. 10. Effect of the MPIC-OPT-ETQ jitter correction. Left: EW ground deformation field computed with MPIC-OPT-ETQ with the jitter correction. Right: EW ground deformation fields computed with Very High Resolution images. Top: Worldview images using the Ampcorr correlator (Barnhart et al., 2019) and bottom: Planet using the Cosi-Corr correlator (Milliner and Donnellan, 2020).

is the choice of the temporal matching range to create the pairs of images. Indeed, this parameter should take into consideration the spatial resolution of the satellite (p), the sensitivity of the matching algorithm (s) and the minimum velocity of the studied object (v_{obj}); therefore the minimal temporal baseline (δt) should satisfy the following criteria:

$$\delta t > \frac{sp}{v_{obj}} \tag{6}$$

The literature reports that the accuracy of most of image correlation algorithm can reach up to $1/10^{th}$ of the pixel size (Heid and Kääb, 2012; Millan et al., 2019). Assuming this precision is reached, in the case of Slumgullion landslide, cycle length of 72 days should be enough to capture the fastest part of the landslide moving at 14 mm.day^{-1} and cycle length of 300 days should capture most of the active zone. However, we show that this precision can be achieved only with a fine tuning of various parameters (Fig. 9). As a consequence, it might be challenging to set up the correct cycle length to retrieve the real ground deformation pattern. Indeed, reducing the cycle length in case of the slow-moving object can prevent the capability of the algorithm to capture the ground deformation. For example in the case of the Slumgullion landslide, if the cycle length is set to less than 300 days and the correlation threshold is low (i.e. C_{min}=0.2), the computed mean velocity is noisy and the landslide deformation is not measured (Fig. 11b). Conversely, if a high correlation threshold is set (i.e. C_{min}=0.7), the pattern of the ground deformation can be retrieved through inversion of the time series (Fig. 11c) but the inverted mean velocity as well as the cumulative ground deformation show lower values (Fig. 11b, c) than the ones obtained with longer cycles (Fig. 8,7a). Moreover, the results with short cycle length show less agreement with in-situ observations. The choice of the temporal baseline to construct the pairing network appears to play an important role on the final results. Currently, a priori knowledge and in-situ measures is needed to confirm the validity of the computed velocity and the ground deformation time series.

In the case of the Alpine glaciers and conversely to Dehecq et al. (2015); Millan et al. (2019); Ali et al. (2020) we did not choose to remove the inter-seasonal pairs from our pairing network. We show that increasing the correlation threshold decreases significantly the magnitude of the seasonal variations (Fig. 9b) especially for the East-West component. Moreover, the inversion of the ground deformation time series should also help to reduce the influence of the sun illumination as demonstrated by Bontemps et al. (2018).

4.3. Choice of the image matching algorithm

Among the different options, the MPIC-OPT services propose two different matching algorithms: MicMac (Rupnik et al., 2017) and GeFolki (Brigot et al., 2016) based on optical flow. We test the performance of both algorithms on the Slumgullion landslide and show that the MicMac algorithm provides ground deformations grids with a better precision than GeFolki (Fig. 8) as well as less noisy ground deformation time series (Fig. 7). Also, we show that the number of outliers is significantly reduced with MicMac over the Ridgecrest fault in comparison with the Cosi-Corr algorithm (Figs. 3,4). These results are in line with previous studies indicating that MicMac usually provides smoother and less noisy results in comparison with other algorithms (Rosu et al., 2015; Le Bivic et al., 2017). However, one of the main advantage of GeFolki is its computational efficiency. Indeed, due to the pixel stepwise interpolation of the input images implemented in MicMac, the

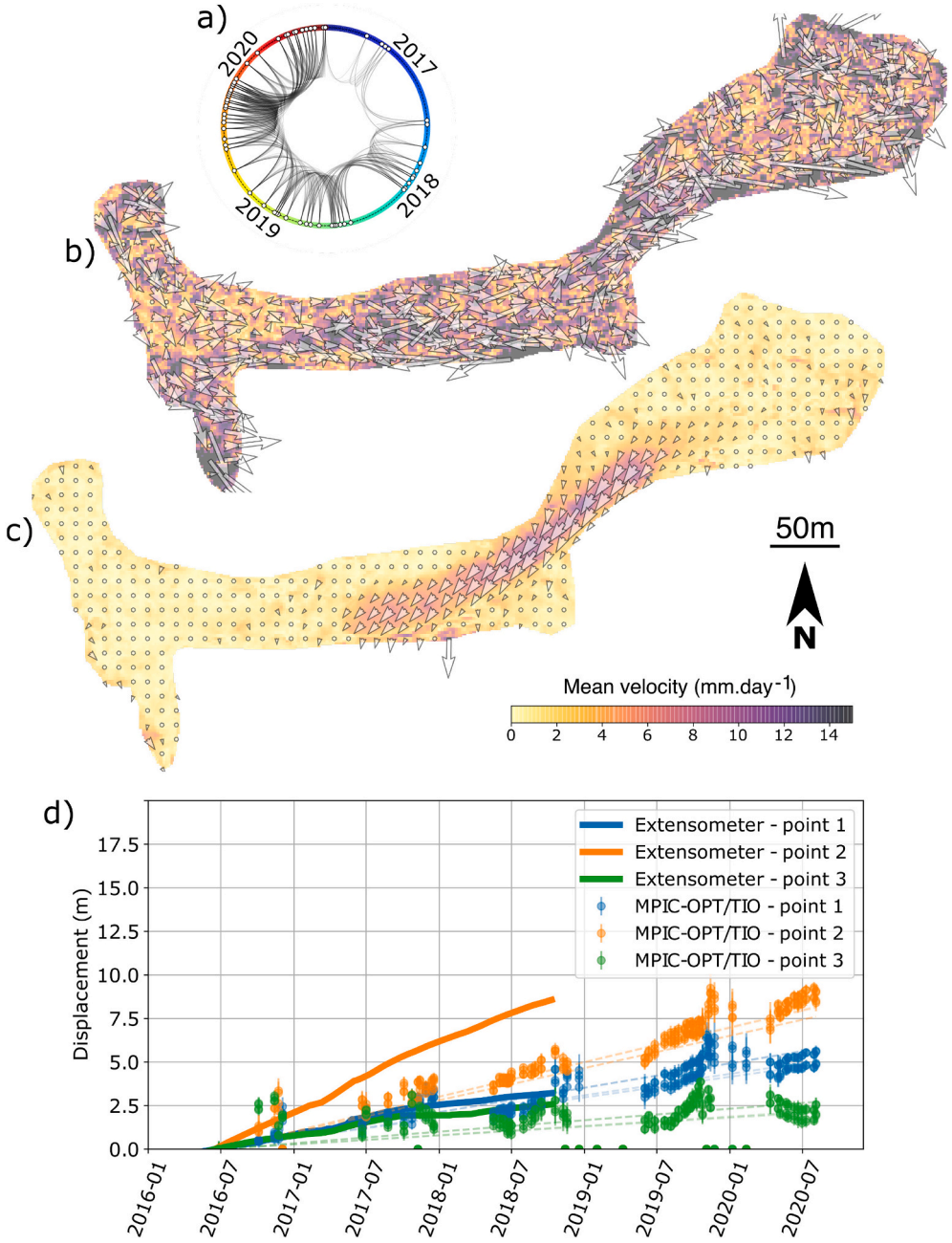

Fig. 11. a) Chord diagram representing the pairing network. Mean surface velocity for the Slumgullion landslide from the stacking of ground deformation grids (MPIC) for b) c_{min}=0.2 and c) c_{min}=0.7. d) shows the inverted ground motion time series at the location of the in-situ extensometers obtained from the run with c_{min}=0.7. See Fig. 7 for the location of the extensometers.

correlation computation is expensive in time and resources while for GeFolki the resolution of the intensity equation is much faster. The GeFolki algorithm is hence a good and inexpensive alternative to obtain quick results and tune the different parameters.

4.4. Optical vs. SAR image correlation for measuring terrain ground deformations

Our results are in agreement with other datasets (e.g. image correlation of high resolution images over the Alps (Millan et al., 2019); UAVSAR image correlation over the Slumgullion landslide (Hu et al., 2020)) and in-situ observations (Figs. 7, 6). The UAVSAR acquisitions have a finer resolution (0.6 m × 1.67 m) than Sentinel-2 (10 m × 10 m) and hence a better precision (i.e. $1/10^{th}$ in the ideal case). Moreover, for each UAVSAR acquisition, four tracks are acquired which allows the inversion of the 3D deformation. However, very high-resolution datasets (optical or SAR), UAVSAR or Ground-Based SAR acquisitions are more expensive options in comparison with the open access of Sentinel-2 data. We show that the exploitation of the Sentinel-2 archive over the Slumgullion landslide provides results comparable to airborne UAVSAR dataset (Hu et al., 2020), high-resolution SAR offset tracking method using COSMO-Skymed data (Amitrano et al., 2019) and Ground-Based InSAR results (Schulz et al., 2017). The Sentinel-2 repetitive acquisition frequency (i.e. 5 days) provides also regular measurements in comparison to the four UAVSAR acquisitions per year.

Due to the ability of the SAR signal to penetrate the clouds, SAR offset-tracking is an interesting method to retrieve high temporal resolution and was tested for glaciers (Mouginot et al., 2017; Lemos et al.,

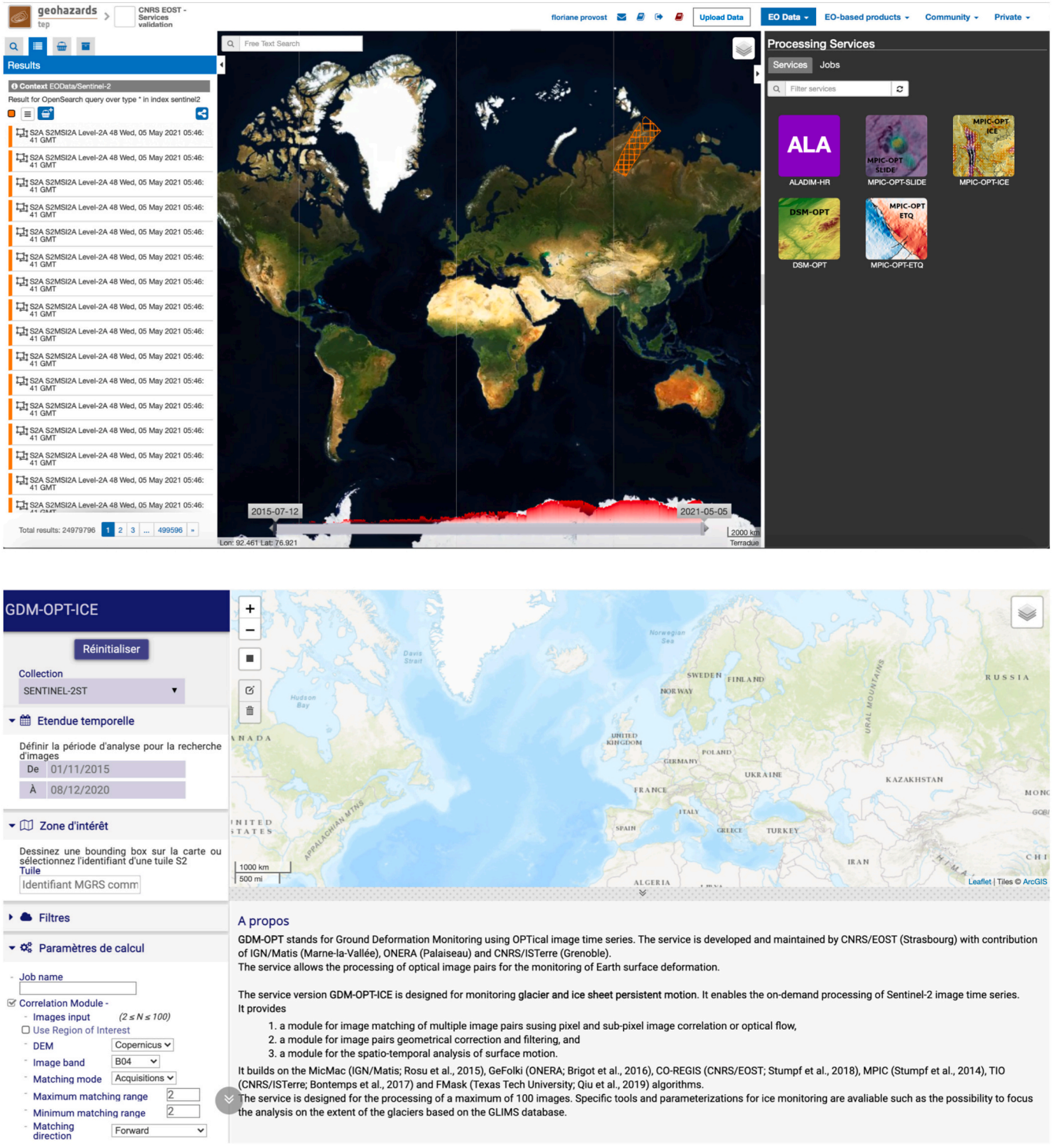

Fig. 12. Screenshots of the Geohazards Exploitation Plateform (GEP; up) and the Form@ter webservice (bottom). Both online platforms provide access to a map, to the Sentinel catalogue and to the MPIC-OPT services.

2018) and landslides (Raucoules et al., 2013; Singleton et al., 2014; Sun and Muller, 2016; Sun et al., 2017; Amitrano et al., 2019) monitoring. However, very few publications reported the use of the Sentinel-1 for landslide monitoring (Xu et al., 2020; Dille et al., 2021). The presence of vegetation and the spatial resolution of Sentinel-1 (5 m × 20 m) makes the application of offset tracking with this free dataset difficult for landslide monitoring but as stated by Dille et al. (2021) not impossible for certain sites. The adaptation of the MPIC service to SAR acquisition is hence considered in future development.

We show that image matching using the Sentinel-2 archive is able to track the motion of various ground deformation pattern from centimeters per day to several meters per day (Fig. 9). Currently, the Sentinel-2 archive offers a complementary measure to InSAR results or other exploitation of the SAR and optical high-resolution acquisitions (Dille et al., 2021). At a regional level, the Sentinel-2 dataset could improve the detection of active landslides as mentioned by Lacroix et al. (2018)

and in a range of ground deformation larger than the one obtained from InSAR datasets (Rosi et al., 2018; Bekaert et al., 2020; Aslan et al., 2020). As the archive will grow with time, using image correlation may allow to access even lower range of ground deformations velocity which represents a potential to jointly exploit the archives of optical and SAR acquisitions and retrieve the ground deformation in three dimensions.

4.5. Access to high performance computing and online environment

The algorithm is deployed on the A2S/High Performance Computing infrastructure of University of Strasbourg (1.5 Tier Mesocentre) allowing optimized and cost effective computation. The MPIC-OPT services and the HPC ressources are accessible by request through the Geohazards Exploitation Platform (GEP: geohazards-tep.eu; Fig. 12a) or the ForM@Ter (French Solid Earth Centre) webservices (www.poleterre solide.fr; Fig. 12b). The GEP is an ESA thematic platform providing access to co-located Earth Observation services and data for the science communities. The GEP is publicly accessible for anyone by registration and services can be used by subscribing to the platform. ESA sponsors the subscription for research projects through the Network Of Resources (https://nor.cloudeo.group/). ForM@Ter is a French initiative to facilitate access to data and contribute to the creation of satellite products and services. It is part of the national Data Infrastructure DataTerra (www.data-terra.org). The algorithm is accessible by ForM@Ter for all the French science community. The use of online environments and HPC resources guarantee an easy access to data catalogue and advanced services in a user-friendly environment and accessible price. The results can also be visualized and are stored online and is catalogued with its input parameters.

5. Conclusion

In this work, we present the new implementation of the Multi-Pairwise Image Correlation for OPTical images algorithm (MPIC-OPT). The algorithm is tailored to compute ground deformation from matching of optical images with two matching algorithms (MicMac, GeFolki). In order to simplify the use of the algorithm for several user communities, the algorithm is accessible through three different services (ETQ, ICE, SLIDE) with different sets of relevant and tunable parameters. The current version of the algorithm ingests Sentinel-2 L1C data and the full image catalogue is available on both platforms. Among the main new functions implemented, we proposed a correction for jitter undulation using a wavelet filter and we added an inversion module based on the Time-series Inversion of Optical images (TIO; Doin et al. (2011); Bontemps et al. (2018)).

The algorithm performances are tested on three different sites: the Ridgecrest fault, the Mont-Blanc alpine glaciers and the Slumgullion landslide. We show the ability to retrieve accurate estimation of the ground deformation for regional (100 km^2) to local regions of interest ($<1km^2$), for diachronic or long-term time series with several acquisitions. We tested the influence of critical parameters on the quality and precision of the terrain ground deformation and its ability to retrieve the ground deformation/velocity time series. We show that the quality of the image correlation depends on the parameters (especially the correlation threshold), the choice of the algorithm and the range of the temporal baselines to create the pairing network.

This study demonstrates the potential of high resolution optical images (such as the Sentinel-2 acquisition) for monitoring slow to rapid horizontal motion and to detect motion patterns that can not be measured with other techniques (InSAR). The algorithm and its implementation on efficient computing environment provides a stable and robust service to exploit the Sentinel-2 archive and contribute to a better understanding and detection of various natural hazards.

CRediT authorship contribution statement

Floriane Provost: Conceptualization, Methodology, Software, Investigation, Validation, Writing – original draft, Writing – review & editing. **David Michéa:** Methodology, Software, Validation. **Jean-Philippe Malet:** Conceptualization, Methodology, Funding acquisition, Supervision, Writing – review & editing. **Enguerran Boissier:** Software. **Elisabeth Pointal:** Software. **André Stumpf:** Conceptualization, Methodology, Software, Writing – review & editing. **Fabrizio Pacini:** Funding acquisition. **Marie-Pierre Doin:** Methodology, Software. **Pascal Lacroix:** Methodology, Writing – review & editing. **Catherine Proy:** Funding acquisition. **Philippe Bally:** Funding acquisition.

Declaration of Competing Interest

The authors declare that they have no known competing financial interests or personal relationships that could have appeared to influence the work reported in this paper.

Acknowledgements

This work was financed by the European Space Agency (ESA) through the Internal Research Fellowship program and the support to the development of the Geohazards Exploitation Platform (GEP), and by the National Centre for Space Studies (CNES) part of the ForM@Ter Solid Earth data infrastructure. The authors would like to thank J. Mouginot, A. Rabatel, A. Dehecq and R. Millan (IGE, Grenoble) for their suggestions on the MPIC-OPT-ICE service and A. Delorme and Y. Klinger (IPGP) for their suggestions on the MPIC-OPT-ETQ service. Further, the authors thank all the members of the French national working group on satellite optical data for terrain motion analysis leaded by CNES for the Data-Terra research e-infrastructure.

References

Ali, E., Xu, W., Ding, X., 2020. Improved optical image matching time series inversion approach for monitoring dune migration in north sinai sand sea: algorithm procedure, application, and validation. ISPRS J. Photogramm. Remote Sens. 164, 106–124. URL. http://www.sciencedirect.com/science/article/pii/S0924271620300952. https://doi.org/10.1016/j.isprsjprs.2020.04.004.

Altena, B., Kääb, A., 2017. Weekly glacier flow estimation from dense satellite time series using adapted optical flow technology. Front. Earth Sci. 5, 53. https://doi.org/10.3389/feart.2017.00053.

Amitrano, D., Guida, R., Dell'Aglio, D., Di Martino, G., Di Martire, D., Iodice, A., Costantini, M., Malvarosa, F., Minati, F., 2019. Long-term satellite monitoring of the slumgullion landslide using space-borne synthetic aperture radar sub-pixel offset tracking. Remote Sens. 11, 369.

Aslan, G., Foumelis, M., Raucoules, D., De Michele, M., Bernardie, S., Cakir, Z., 2020. Landslide mapping and monitoring using persistent scatterer interferometry (psi) technique in the french alps. Remote Sens. 12, 1305.

Avouac, J.P., Ayoub, F., Leprince, S., Konca, O., Helmberger, D.V., 2006. The 2005, mw 7.6 kashmir earthquake: sub-pixel correlation of aster images and seismic waveforms analysis. Earth Planet. Sci. Lett. 249, 514–528.

Ayoub, F., Leprince, S., Binet, R., Lewis, K.W., Aharonson, O., Avouac, J.P., 2008. Influence of camera distortions on satellite image registration and change detection applications. In: IGARSS 2008–2008 IEEE International Geoscience and Remote Sensing Symposium. IEEE pp. II–1072.

Barnhart, W.D., Hayes, G.P., Gold, R.D., 2019. The july 2019 ridgecrest, california, earthquake sequence: kinematics of slip and stressing in cross-fault ruptures. Geophys. Res. Lett. 46, 11859–11867.

Bekaert, D.P., Handwerger, A.L., Agram, P., Kirschbaum, D.B., 2020. Insar-based detection method for mapping and monitoring slow-moving landslides in remote regions with steep and mountainous terrain: an application to Nepal. Remote Sens. Environ. 249, 111983.

Bindschadler, R., Scambos, T., 1991. Satellite-image-derived velocity field of an antarctic ice stream. Science 252, 242–246.

Bontemps, N., Lacroix, P., Doin, M.P., 2018. Inversion of deformation fields time-series from optical images, and application to the long term kinematics of slow-moving landslides in peru. Remote Sens. Environ. 210, 144–158. URL. http://www.sciencedirect.com/science/article/pii/S0034425718300282. https://doi.org/10.1016/j.rse.2018.02.023.

Brigot, G., Colin-Koeniguer, E., Plyer, A., Janez, F., 2016. Adaptation and evaluation of an optical flow method applied to coregistration of forest remote sensing images. IEEE J. Select. Top. Appl. Earth Observ. Remote Sens. 9, 2923–2939.

Chen, K., Avouac, J.P., Aati, S., Milliner, C., Zheng, F., Shi, C., 2020. Cascading and pulse-like ruptures during the 2019 ridgecrest earthquakes in the eastern California shear zone. Nat. Commun. 11, 1–8.

Coe, J.A., Ellis, W.L., Godt, J.W., Savage, W.Z., Savage, J.E., Michael, J., Kibler, J.D., Powers, P.S., Lidke, D.J., Debray, S., 2003. Seasonal movement of the slumgullion landslide determined from global positioning system surveys and field instrumentation, july 1998–march 2002. Eng. Geol. 68, 67–101.

Cournet, M., Giros, A., Dumas, L., Delvit, J., Greslou, D., Languille, F., Blanchet, G., May, S., Michel, J., 2016. 2d sub-pixel disparity measurement using qpec/medicis. Int. Arch. Photogram. Remote Sens. Spat. Inform. Sci. 41.

Dehecq, A., Gourmelen, N., Trouve, E., 2015. Deriving large-scale glacier velocities from a complete satellite archive: application to the pamir–karakoram–himalaya. Remote Sens. Environ. 162, 55–66. URL. http://www.sciencedirect.com/science/article/pii/S0034425715000553. https://doi.org/10.1016/j.rse.2015.01.031.

Dille, A., Kervyn, F., Handwerger, A.L., d'Oreye, N., Derauw, D., Bibentyo, T.M., Samsonov, S., Malet, J.P., Kervyn, M., Dewitte, O., 2021. When image correlation is needed: unravelling the complex dynamics of a slow-moving landslide in the tropics with dense radar and optical time series. Remote Sens. Environ. 258, 112402.

Ding, C., Feng, G., Li, Z., Shan, X., Du, Y., Wang, H., 2016. Spatio-temporal error sources analysis and accuracy improvement in landsat 8 image ground displacement measurements. Remote Sens. 8, 937.

Doin, M.P., Guillaso, S., Jolivet, R., Lasserre, C., Lodge, F., Ducret, G., Grandin, R., 2011. Presentation of the small baseline nsbas processing chain on a case example: The etna deformation monitoring from 2003 to 2010 using envisat data. In: Proceedings of the Fringe symposium, ESA SP-697, Frascati, Italy, pp. 3434–3437.

DuRoss, C.B., Gold, R.D., Dawson, T.E., Scharer, K.M., Kendrick, K.J., Akciz, S.O., Angster, S.J., Bachhuber, J., Bacon, S., Bennett, S.E.K., Blair, L., Brooks, B.A., Bullard, T., Burgess, W.P., Chupik, C., DeFrisco, M., Delano, J., Dolan, J.F., Frost, E., Graehl, N., Haddon, E.K., Hatem, A.E., Hernandez, J.L., Hitchcock, C., Hudnut, K., Jobe, J.T., Koehler, R., Kozaci, O., Ladinsky, T., Madugo, C., McPhillips, D.S., Milliner, C., Morelan, A., Olson, B., Patton, J., Philibosian, B., Pickering, A.J., Pierce, I., Ponti, D.J., Seitz, G., Spangler, E., Swanson, B., Thomas, K., Treiman, J., Valencia, F., Williams, A., Zinke, R., 2020. Surface displacement distributions for the July 2019 Ridgecrest, California, earthquake ruptures. Bull. Seismol. Soc. Am. 110 (4), 1400–1418. https://doi.org/10.1785/0120200058.

Fahnestock, M., Scambos, T., Bindschadler, R., 1992. Semi-automated ice velocity determination from satellite imagery. Eos 73, 493.

Fahnestock, M., Scambos, T., Moon, T., Gardner, A., Haran, T., Klinger, M., 2016. Rapid large-area mapping of ice flow using landsat 8. Remote Sens. Environ. 185, 84–94.

Fielding, E.J., Liu, Z., Stephenson, O.L., Zhong, M., Liang, C., Moore, A., Yun, S.H., Simons, M., 2020. Surface deformation related to the 2019 m w 7.1 and 6.4 ridgecrest earthquakes in California from gps, sar interferometry, and sar pixel offsets. Seismol. Res. Lett. 91 (4), 2035–2046. https://doi.org/10.1785/0220190302.

Fleming, R.W., US, G.S., 1999. Map and Description of the Active Part of the Slumgullion Landslide, Hinsdale County, Colorado. US Department of the Interior, US Geological Survey.

Gardner, A.S., Fahnestock, M., Scambos, T.A., 2019. Its_live regional glacier and ice sheet surface velocities. In: Data Archived at National Snow and Ice Data Center.

Gascon, F., Bouzinac, C., Thépaut, O., Jung, M., Francesconi, B., Louis, J., Lonjou, V., Lafrance, B., Massera, S., Gaudel-Vacaresse, A., 2017. Copernicus sentinel-2a calibration and products validation status. Remote Sens. 9, 584. https://doi.org/10.3390/rs9060584.

Gens, R., Van Genderen, J.L., 1996. Review article sar interferometry–issues, techniques, applications. Int. J. Remote Sens. 17, 1803–1835.

Geudtner, D., Torres, R., Snoeij, P., Davidson, M., Rommen, B., 2014. Sentinel-1 system capabilities and applications. In: 2014 IEEE Geoscience and Remote Sensing Symposium, pp. 1457–1460. https://doi.org/10.1109/IGARSS.2014.6946711.

Guerriero, L., Di Martire, D., Calcaterra, D., Francioni, M., 2020. Digital image correlation of google earth images for earth's surface displacement estimation. Remote Sens. 12, 3518.

Heid, T., Kääb, A., 2012. Evaluation of existing image matching methods for deriving glacier surface displacements globally from optical satellite imagery. Remote Sens. Environ. 118, 339–355. URL. http://www.sciencedirect.com/science/article/pii/S0034425711004214. https://doi.org/10.1016/j.rse.2011.11.024.

Horn, B.K., Schunck, B.G., 1981. Determining optical flow. In: Techniques and Applications of Image Understanding, International Society for Optics and Photonics, pp. 319–331.

Hu, X., Bürgmann, R., Schulz, W.H., Fielding, E.J., 2020. Four-dimensional surface motions of the slumgullion landslide and quantification of hydrometeorological forcing. Nat. Commun. 11, 1–9.

Kääb, A., Vollmer, M., 2000. Surface geometry, thickness changes and flow fields on creeping mountain permafrost: automatic extraction by digital image analysis. Permafr. Periglac. Process. 11, 315–326.

Kääb, A., Winsvold, S.H., Altena, B., Nuth, C., Nagler, T., Wuite, J., 2016. Glacier remote sensing using sentinel-2. Part i: radiometric and geometric performance, and application to ice velocity. Remote Sens. 8, 598.

Kirst, C., Skriabine, S., Vieites-Prado, A., Topilko, T., Bertin, P., Gerschenfeld, G., Verny, F., Topilko, P., Michalski, N., Tessier-Lavigne, M., et al., 2020. Mapping the fine-scale organization and plasticity of the brain vasculature. Cell 180, 780–795.

Lacroix, P., Bièvre, G., Pathier, E., Kniess, U., Jongmans, D., 2018. Use of sentinel-2 images for the detection of precursory motions before landslide failures. Remote Sens. Environ. 215, 507–516. URL. http://www.sciencedirect.com/science/article/pii/S0034425718301433. https://doi.org/10.1016/j.rse.2018.03.042.

Lacroix, P., Araujo, G., Hollingsworth, J., Taipe, E., 2019. Self-entrainment motion of a slow-moving landslide inferred from landsat-8 time series. J. Geophys. Res. Earth Surf. 124, 1201–1216.

Le Bivic, R., Allemand, P., Quiquerez, A., Delacourt, C., 2017. Potential and limitation of spot-5 ortho-image correlation to investigate the cinematics of landslides: the example of "mare à poule d'eau" (réunion, France). Remote Sens. 9 https://doi.org/10.3390/rs9020106.

Lemos, A., Shepherd, A., McMillan, M., Hogg, A.E., Hatton, E., Joughin, I., 2018. Ice velocity of jakobshavn isbræ, petermann glacier, nioghalvfjerdsfjorden, and zachariæ isstrøm, 2015–2017, from sentinel 1-a/b sar imagery. Cryosphere 12, 2087–2097.

Lenzano, M.G., Lannutti, E., Toth, C., Rivera, A., Lenzano, L., 2018. Detecting glacier surface motion by optical flow. Photogramm. Eng. Remote. Sens. 84, 33–42.

Leprince, S., Barbot, S., Ayoub, F., Avouac, J.P., 2007. Automatic and precise orthorectification, coregistration, and subpixel correlation of satellite images, application to ground deformation measurements. IEEE Trans. Geosci. Remote Sens. 45, 1529–1558.

Leprince, S., Musé, P., Avouac, J.P., 2008. In-flight ccd distortion calibration for pushbroom satellites based on subpixel correlation. IEEE Trans. Geosci. Remote Sens. 46, 2675–2683.

López-Quiroz, P., Doin, M.P., Tupin, F., Briole, P., Nicolas, J.M., 2009. Time series analysis of mexico city subsidence constrained by radar interferometry. J. Appl. Geophys. 69, 1–15. URL. http://www.sciencedirect.com/science/article/pii/S0926985109000251. https://doi.org/10.1016/j.jappgeo.2009.02.006. advances in SAR Interferometry from the 2007 Fringe Workshop.

Massonnet, D., Feigl, K.L., 1998. Radar interferometry and its application to changes in the earth's surface. Rev. Geophys. 36, 441–500.

Messerli, A., Grinsted, A., 2015. Image georectification and feature tracking toolbox: Imgraft. In: Geoscientific Instrumentation, Methods and Data Systems, 4, p. 23.

Michel, R., Avouac, J.P., Taboury, J., 1999. Measuring ground displacements from sar amplitude images: application to the landers earthquake. Geophys. Res. Lett. 26, 875–878.

Millan, R., Mouginot, J., Rabatel, A., Jeong, S., Cusicanqui, D., Derkacheva, A., Chekki, M., 2019. Mapping surface flow velocity of glaciers at regional scale using a multiple sensors approach. Remote Sens. 11, 2498. https://doi.org/10.3390/rs11212498.

Milliner, C., Donnellan, A., 2020. Using daily observations from planet labs satellite imagery to separate the surface deformation between the 4 july m w 6.4 foreshock and 5 july m w 7.1 mainshock during the 2019 ridgecrest earthquake sequence. Seismol. Res. Lett. 91 (4), 1986–1997. https://doi.org/10.1785/0220190271.

Mouginot, J., Rignot, E., Scheuchl, B., Millan, R., 2017. Comprehensive annual ice sheet velocity mapping using landsat-8, sentinel-1, and radarsat-2 data. Remote Sens. 9, 364.

Münch, B., Trtik, P., Marone, F., Stampanoni, M., 2009. Stripe and ring artifact removal with combined wavelet–fourier filtering. Opt. Express 17, 8567–8591.

Nagy, T., Andreassen, L.M., Duller, R.A., Gonzalez, P.J., 2019. Sendit: the sentinel-2 displacement toolbox with application to glacier surface velocities. Remote Sens. 11 https://doi.org/10.3390/rs11101151.

Qiu, S., Zhu, Z., He, B., 2019. Fmask 4.0: improved cloud and cloud shadow detection in landsats 4–8 and sentinel-2 imagery. Remote Sens. Environ. 231, 111205. URL.

Racoviteanu, A., 2007. Glims Glacier Database, Version 1 analysis ids 60827–61235.

Raucoules, D., De Michele, M., Mallet, J., 2013. Mapping La Valette landslide (French Alps) displacement using high resolution SAR image correlation. In: ESA Living Planet Symposium 2013, Edinburgh, United Kingdom. URL. https://hal-brgm.archives-ouvertes.fr/hal-00846898. http://www.livingplanet2013.org/abstracts/843509.htm.

Renier, N., Adams, E.L., Kirst, C., Wu, Z., Azevedo, R., Kohl, J., Autry, A.E., Kadiri, L., Venkataraju, K.U., Zhou, Y., et al., 2016. Mapping of brain activity by automated volume analysis of immediate early genes. Cell 165, 1789–1802.

Rosi, A., Tofani, V., Tanteri, L., Stefanelli, C.T., Agostini, A., Catani, F., Casagli, N., 2018. The new landslide inventory of tuscany (Italy) updated with ps-insar: geomorphological features and landslide distribution. Landslides 15, 5–19.

Ross, Z.E., Idini, B., Jia, Z., Stephenson, O.L., Zhong, M., Wang, X., Zhan, Z., Simons, M., Fielding, E.J., Yun, S.H., Hauksson, E., Moore, A.W., Liu, Z., Jung, J., 2019. Hierarchical interlocked orthogonal faulting in the 2019 ridgecrest earthquake sequence. Science 366, 346–351. URL. https://science.sciencemag.org/content/366/6463/346. https://doi.org/10.1126/science.aaz0109. arXiv. https://science.sciencemag.org/content/366/6463/346.full.pdf.

Rosu, A.M., Pierrot-Deseilligny, M., Delorme, A., Binet, R., Klinger, Y., 2015. Measurement of ground displacement from optical satellite image correlation using the free open-source software micmac. ISPRS J. Photogramm. Remote Sens. 100, 48–59. URL. http://www.sciencedirect.com/science/article/pii/S0924271614000653. https://doi.org/10.1016/j.isprsjprs.2014.03.002. high-Resolution Earth Imaging for Geospatial Informationm.

Rupnik, E., Daakir, M., Deseilligny, M.P., 2017. Micmac–a free, open-source solution for photogrammetry. In: Open Geospatial Data, Software and Standards, 2, pp. 1–9.

Scambos, T.A., Dutkiewicz, M.J., Wilson, J.C., Bindschadler, R.A., 1992. Application of image cross-correlation to the measurement of glacier velocity using satellite image data. Remote Sens. Environ. 42, 177–186.

Scherler, D., Leprince, S., Strecker, M.R., 2008. Glacier-surface velocities in alpine terrain from optical satellite imagery–accuracy improvement and quality assessment. Remote Sens. Environ. 112, 3806–3819.

Schulz, W.H., McKenna, J.P., Kibler, J.D., Biavati, G., 2009. Relations between hydrology and velocity of a continuously moving landslide–evidence of pore-pressure feedback regulating landslide motion? Landslides 6, 181–190.

Schulz, W., Coe, J., Shurtleff, B., Panosky, J., Farina, P., Ricci, P., Barsacchi, G., 2012. Kinematics of the slumgullion landslide revealed by ground-based insar surveys. In: Landslides and Engineered Slopes, Protecting Society through Improved Understanding, 2, pp. 1273–1279.

Schulz, W.H., Coe, J.A., Ricci, P.P., Smoczyk, G.M., Shurtleff, B.L., Panosky, J., 2017. Landslide kinematics and their potential controls from hourly to decadal timescales: insights from integrating ground-based insar measurements with structural maps and long-term monitoring data. Geomorphology 285, 121–136.

Singleton, A., Li, Z., Hoey, T., Muller, J.P., 2014. Evaluating sub-pixel offset techniques as an alternative to d-insar for monitoring episodic landslide movements in vegetated terrain. Remote Sens. Environ. 147, 133–144.

Stumpf, A., Malet, J.P., Puissant, A., Travelletti, J., 2016. Monitoring of earth surface motion and geomorphologic processes by optical image correlation. In: Baghdadi, N., Zribi, M. (Eds.), Land Surface Remote Sensing. Elsevier, pp. 147–190. URL.

Stumpf, A., Malet, J.P., Delacourt, C., 2017. Correlation of satellite image time-series for the detection and monitoring of slow-moving landslides. Remote Sens. Environ. 189, 40–55. URL. http://www.sciencedirect.com/science/article/pii/S0034425716304394. https://doi.org/10.1016/j.rse.2016.11.007.

Stumpf, A., Michéa, D., Malet, J.P., 2018. Improved co-registration of sentinel-2 and landsat-8 imagery for earth surface motion measurements. Remote Sens. 10, 160. https://doi.org/10.3390/rs10020160.

Sun, L., Muller, J.P., 2016. Evaluation of the use of sub-pixel offset tracking techniques to monitor landslides in densely vegetated steeply sloped areas. Remote Sens. 8, 659.

Sun, L., Muller, J.P., Chen, J., 2017. Time series analysis of very slow landslides in the three gorges region through small baseline sar offset tracking. Remote Sens. 9, 1314.

Teshima, Y., Iwasaki, A., 2008. Correction of attitude fluctuation of terra spacecraft using aster/swir imagery with parallax observation. IEEE Trans. Geosci. Remote Sens. 46, 222–227.

Van Wyk de Vries, M., Wickert, A.D., 2020. Glacier image velocimetry: an open-source toolbox for easy and rapid calculation of high-resolution glacier-velocity fields. In: The Cryosphere Discussions 2020, pp. 1–31. URL. https://tc.copernicus.org/preprints/tc-2020-204/. https://doi.org/10.5194/tc-2020-204.

Vogel, C., Bauder, A., Schindler, K., 2012. Optical flow for glacier motion estimation. In: Proceedings of the 22nd ISPRS Congress, Melbourne, Australia.

Wang, K., Bürgmann, R., 2020. Co- and early postseismic deformation due to the 2019 ridgecrest earthquake sequence constrained by Sentinel-1 and COSMO-SkyMed SAR data. Seismol. Res. Lett. https://doi.org/10.1785/0220190299.

Wulder, M.A., White, J.C., Loveland, T.R., Woodcock, C.E., Belward, A.S., Cohen, W.B., Fosnight, E.A., Shaw, J., Masek, J.G., Roy, D.P., 2016. The global landsat archive: status, consolidation, and direction. Remote Sens. Environ. 185, 271–283.

Xu, X., Sandwell, D.T., Smith-Konter, B., 2020. Coseismic displacements and surface fractures from sentinel-1 insar: 2019 ridgecrest earthquakes. Seismol. Res. Lett. 91 (4), 1979–1985. https://doi.org/10.1785/0220190275.

Yamazaki, D., Ikeshima, D., Tawatari, R., Yamaguchi, T., O'Loughlin, F., Neal, J.C., Sampson, C.C., Kanae, S., Bates, P.D., 2017. A high-accuracy map of global terrain elevations. Geophys. Res. Lett. 44, 5844–5853.

Ye, Z., Xu, Y., Tong, X., Zheng, S., Zhang, H., Xie, H., Stilla, U., 2019. Estimation and analysis of along-track attitude jitter of ziyuan-3 satellite based on relative residuals of tri-band multispectral imagery. ISPRS J. Photogramm. Remote Sens. 158, 188–200. URL. http://www.sciencedirect.com/science/article/pii/S0924271619302497. https://doi.org/10.1016/j.isprsjprs.2019.10.012.